Hierarchical approach for uncertainty quantification and reliability assessment of guided wave based structural health monitoring

Nan Yue*, M.H. Aliabadi

Department of Aeronautics, Imperial College London, London, UK

Abstract

In this paper, a hierarchical approach is proposed for the design and assessment of a guided wave-based structural health monitoring (GWSHM) system for the detection and localization of barely visible impact damage (BVID) in composite airframe structures. The hierarchical approach provides a systemic and practical way to establish GWSHM systems for different structures in the presence of uncertainties and to quantify system performance. The proposed approach is carried out in four steps: (1) determine optimal sensor placement for the target structure and its plausible impact scenarios, (2) set detection threshold for global damage index based on the noise level present in the required environmental and operations conditions, (3) detect damage in critical locations and quantify detection performance by calculating probability of detection (POD), probability of false alarm (PFA) and detection accuracy and (4) locate the detected damage while also quantify the accuracy of location estimation and the probability of correctly indicating if the damage is in an area critical to the integrity of the structure. The proposed approach is demonstrated in aircraft CFRP structures from coupon level (simple flat panels) to sub-component level (large flat panel with multiple CFRP stringers and aluminium frames) for the detection and localisation of BVID.

Keywords: Ultrasonic guided wave, Structural health monitoring, Airframe, Composite, Uncertainty quantification, Barely visible impact damage

1. Introduction

The transformation of aircraft maintenance from the current schedule-based strategy to a faster, smarter and automated way of maintenance is inevitable in the age of Industry 4.0. Great effort has been directed in both academia and industry over the past few decades towards the research and development of Structural Health Monitoring (SHM) as a new way of maintenance that aims for the efficient and continuous assessment of structural integrity[1, 2]. However, there are still many challenges left in developing a SHM system for commercial aircraft. These challenges include not only in the development of sensor network and the interpretation of sensor data, but also in the establishment of validation methods and certification criteria for the commercial use of SHM systems[3].

Ultrasonic guided wave has been recognised to be practical in interrogating large plate-like structures due to its capability to propagate over long distances with minimal energy loss[4, 5]. Guided wave based structural health monitoring (GWSHM) systems provide information on structural integrity based on measurements obtained from transducers such as piezoelectric and fibre optic sensors. These sensor measurements are influenced by changes in environmental and operational conditions, as well as the presence of electrical noise. This causes a significant level of uncertainty in the sensor measurements which cannot be ignored and requires the application of statistical analysis techniques to take into account their

---

*Corresponding author:
Nan Yue, Department of Aeronautics, Imperial College London, South Kensington Campus, Exhibition Road, SW7 2AZ, London, UK.
Email: nan.yue14@imperial.ac.uk

effects. To add further complication, the environmental and operational conditions can have different effects on guided waves depending on the material as well as the type of damage present [6]. In order to achieve highly accurate damage identification using GWSHM systems under the required service conditions for an aircraft, the uncertainties due to environmental and operational conditions mentioned earlier, as well as the uncertainties in the characteristics of the damage must be quantified for the range of materials present in the aircraft.

To obtain information regarding the existence of structural damage, guided wave features that are sensitive to the presence of damage can be extracted and fused to form a damage index that represents the current state of the integrity of the structure. A threshold value for the damage index can be used to distinguish a damaged state from an undamaged state. This threshold value is determined based on a certain level of statistical confidence in the sensor measurement under the presence of uncertainty caused by random and systemic noise.

The methods used for assessing the reliability of damage detection for SHM systems can be divided into two main groups[7]: (1) methods that conduct a signal response to damage size analysis; (2) methods can conduct a hit/miss analysis. The former originates from the guidelines for conventional non-destructive inspection (NDI) techniques[8]. It applies if the system provides a continuous signal response correlated with damage size, and reports the probability of detection and confidence limit related to damage size, known as POD(a) curve. Hit/miss analysis applies when the system returns binary results on whether or not a defect is present, and is used in binary classification problems in many fields such as machine learning and signal detection. Hit-miss analysis quantifies the probability of four detection outcomes: true positive, false positive, false negative and true negative. These four probability are closely related to the decision threshold, and this relationship is illustrated by a Receiver operating characteristic (ROC) curve which plots probability of true positive against probability of false negative as the threshold value varies[9].

Many studies have been dedicated to the adoption of NDI approached for GWSHM systems for damage identification at damage prone locations, such as bolted joints susceptible to the forming of cracks, and bonded joints vulnerable to debonding.[11]. Under the NDI approach, the POD(a) curve is derived from independent inspection data for different defect sizes[8]. However, in the case of SHM systems, sensor measurements are repeatedly taken from the host structure. Therefore the data is not independent and a POD(a) curve cannot be calculated. Schubert Kabban et al. [10] modified the POD(a) approach to handle repeated measurement data, which enabled the application of the POD(a) approach for SHM systems. Another limitation of the POD(a) approach is that the defect is solely represented by its size. Many SHM techniques, especially guided wave based techniques are also sensitive to the shape of the defect as well as its position relative to the sensors. Gianneo et al.[12] investigated the influence of multiple crack parameters in Aluminium on POD curves. It was shown that defect parameters including crack size, guided wave incident angle and reception angle have different levels of influence on the POD(a) curves and should be considered separately. Furthermore, the biggest challenge in establishing a POD(a) curve is arguably the tremendous amount of data required, including defects of different types, sizes, orientations, and at different locations. Moriot et al. [13] proposed a model assisted approach assessing guided wave based detection and localisation of simulated damage. Damage detection was evaluated using a POD(a) approach. Although experimental results from magnetic discs under consistent environmental conditions and FE simulated damage on Aluminium plate agreed well, the simplified damage characteristics are unlikely to be representative of actual damage. Yue et al. [14] proposed an empirical model to describe the damage detectability of guided waves in a pitch-catch sensor configuration. The model considered guided wave damping and wave-damage interaction, which provided a qualitative spacial distribution of probability of detecting damage in various locations.

An important advantage of GWSHM systems over conventional NDI techniques is their capability to effectively detect and localize damage in a large structure with minimum labour or machine assistance. This is particularly beneficial in the case where damage can be distributed in the structure, such as

the damage caused by impact. The assessment of a GWSHM system with a POD(a)approach assumes that the GWSHM system is equivalent to conventional NDI techniques. This ignores the advantage in automation that a GWSHM system provides. An example where the POD(a) approach might not be practical for GWSHM reliability assessment is identifying impact damage in CFRP laminate airframe structures. Unlike metallic materials where impact typically causes a visible dent or scratch, an impact event on composite materials can cause a mixture of fibre breakage, matrix cracking and delamination but remain nearly intact on the surface. If the POD(a) approach is applied, multiple variables will have to be introduced for POD curves in order to comprehend the complexity of the problem caused by diverse CFRP structure design, the complicated damage scenarios and material dependent guided wave characteristics.

Instead of following the POD(a) approach, many studies have assessed the reliability of SHM systems using a hit/miss approach. Nichols et al.[15] and Lu and Michaels[16] used ROC curves to effectively evaluate damage detection performance for single damage. Flynn et al. [17] evaluated the performance of their GWSHM when detecting multiple through thickness holes in a stiffened aluminium panel using a modified ROC analysis. Monaco et al.[7] considered the probability of detection and probability of false alarm when setting the threshold for detecting impact damage in a CFRP laminate using GWSHM.

This paper is focused on detecting the largest barely visible impact damage (BVID) in different CFRP composite airframe structures and hence the hit/miss analysis is used for quantifying the reliability of damage detection.

Once the presence of damage is detected, its location can be estimated. The localisation of damage can be important when investigating a large area or checking for damage at critical areas that can greatly compromise structural integrity (such as the bondline between the skin and a stiffener). A number of existing damage imaging methods can be used for estimating the damage location, such as the reconstruction algorithm for probabilistic inspection of defects(RAPID)[18], delay-an-sum (DAS)[19], energy arrival[20], Rayleigh maximum likelihood estimation (RMLE) [21] and Bayesian approaches[22][23]. To assess localization performance, Flynn[21] proposed two approaches, probability of location estimation error and Gaussian estimation. Moriot et al.[13] demonstrated the localisation of simulated damage and artificial damage on an aluminium plate using DAS with probability of location estimation error. In this work, two novel approaches for localisation performance are proposed, one provides a more intuitive measure of localisation accuracy, the other represents ability of indicating damage presence in critical locations.

So far, most of the studies in uncertainty quantification and reliability assessment of GWSHM systems for CFRP structures have been carried out for simple isotropic plates. The issues with assessing GWSHM for damage identification in large and complicated composite structures are yet to be addressed. These issues include, but are not limited to, the effects of anisotropic material properties, greater dampening, and more complicated and harder to detect damage types. An appropriate approach is required to assess the functionality of the designed GWHSM system under intended environmental and operational conditions.

This paper proposes a novel hierarchical approach for GWSHM design and assessment for the detection and localisation of BVID in CFRP composite airframe structures. The design process of an GWSHM system considers the placement of transducers, estimation of noise level during the monitoring condition, and the selection of damage characterisation strategy and criteria. The damage detection performance is quantified by probability of detection and probability of false alarm as well as the overall detection accuracy while the damage localisation performance is assessed by the accuracy of the damage localisation estimates as well as probability of correct indication of damage in critical areas. The proposed approach is applied for identifying BVID in CFRP airframe structures at difference scales, including simple CFRP panels, CFRP panels with single CFRP stiffener and CFRP panels with multiple CFRP and aluminium stiffeners.

2. Hierarchical approach

This section present an overview of the proposed hierarchical approach to GWSHM system design and performance quantification, followed by the methodology used in each level of the hierarchy. Figure 1 presents a schematic of the proposed hierarchical approach for a general plate-like structure.

Figure 1: Hierarchical approach
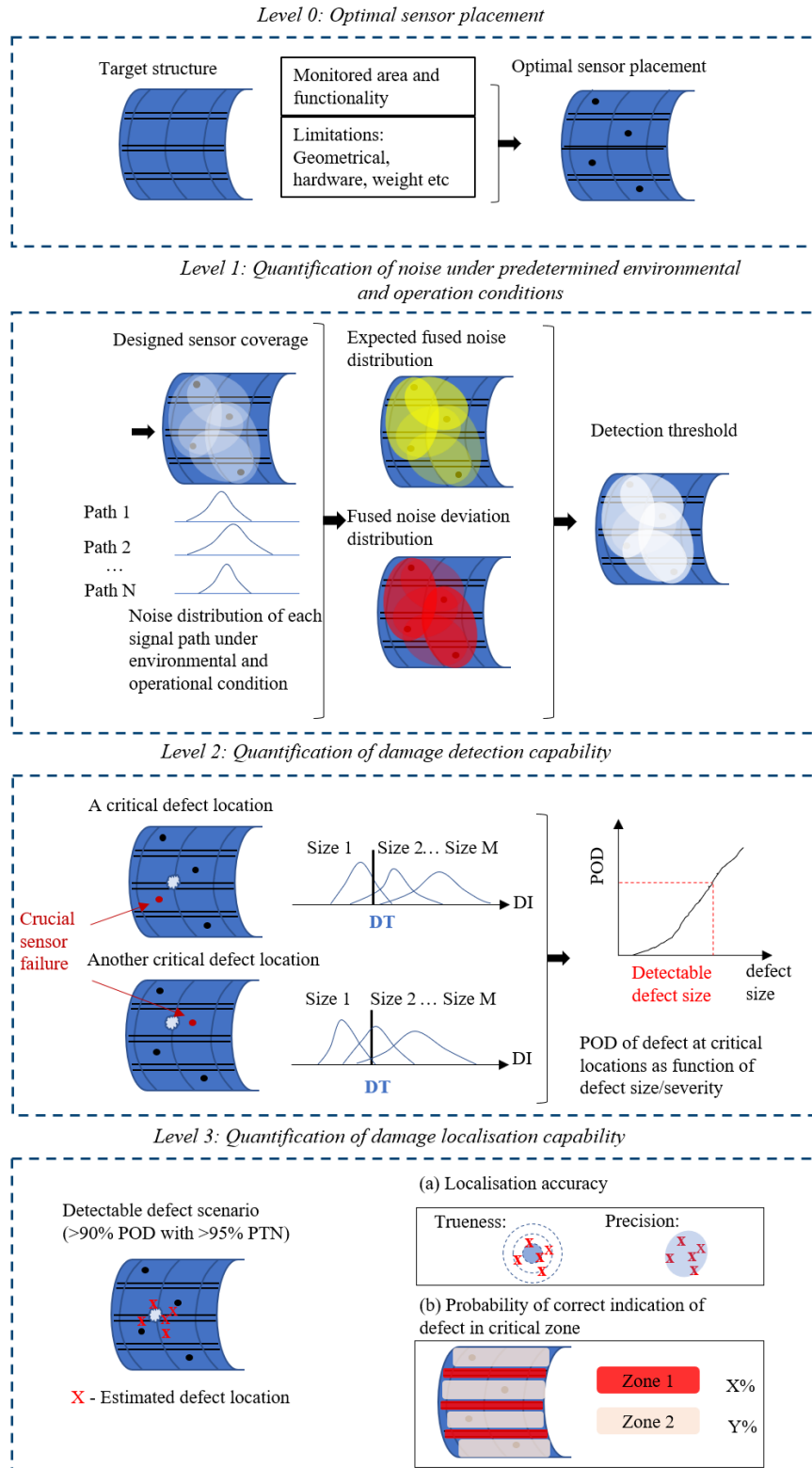
The considerations in each level are briefly introduced as follows:

Level 0: Optimal sensor placement. For the target CFRP aircraft structure and its damage scenarios, a guided wave SHM system can be designed to achieve effective identification of damage while minimise the overall cost. The costs associated with an industrial structural health monitoring systems can be categorized as implementation costs and in-service costs. There is a significant cost in development of advanced technical capabilities for making the integration of sensors in modern composite structures practical and efficient so as to facilitate industrialization and certification. The implementation cost (i.e. weight, data handling, data fusion, power consumption, etc.) can be minimized by optimising sensor positions and by optimising sensor installation procedure during component manufacture. The achievement of this objective should be measured by conducting a detailed cost assessment of the additional manufacturing costs associated with sensor integration including all aspects of the certification process. Sensor integration costs is an important component in the full assessment of operative costs of the SHM-equipped aircraft.

Level 1: Quantification of noise under environmental and operational conditions. The environmental and operational conditions (EOC) under which the GWSHM system will be functioning is pre-defined according to the application requirement. The variability in damage-sensitive guided wave features can then be quantified based on a number of measurements taken at the pristine state of the monitored structure at the pre-defined EOC. The damage sensitive features from individual sensor pairs are then fused according to sensor coverage distributions by taking the average value of the damage sensitive feature from sensor pairs that cover each position. Measures of the fused damage sensitive feature can then be derived in the form of (i) expected fused noise distribution and (ii) fused noise deviation distribution. The former describes the average value of noise and the latter is a measure of noise variability. The positions on the structure where the sensor coverage is high will have reduced variability. In other words, the more available guided wave paths at a position, the more certain is the estimation of damage existence at that position. A global damage index (GDI) indicating the integrity state of the monitored structure is derived from the sensor network and a detection threshold can be determined based on the uncertainty of GDI in pristine state due to environmental and operational conditions.

Level 2: Quantification of damage detection capability. With the detection threshold determined at Level 1, the damage detection can be performed in the pre-defined environmental and operating conditions of GWSHM. Probability of false alarm (PFA) and probability of detection (POD) are calculated using hit-miss analysis to quantify the detection reliability. PFA indicates the chance of false calls in the varying environmental and operation conditions where SHM is designed to be operating, while POD is dependent on the nature and the location of the damage and is expected to be different for different damage scenarios. The most conservative approach for SHM design is to consider the worst-case scenario (the most critical damage location on the structure). The structural damage are introduced at critical locations and the detection performance is evaluated by POD. If the probability of detecting damage at critical locations is below an acceptable value, it might be improved by: increasing the number of sensors; constraining the defined GWSHM operational conditions; compensating for the damage unrelated variation in damage sensitive guided wave features; accepting a higher probability of false alarm by lowering the detection threshold or by accepting a greater detectable damage size (assuming POD monotonically increases with damage size/severity).

System robustness. Degradation or failure of sensors is unavoidable during long term monitoring. According to the redundant design concept, in the event of sensor malfunction, the SHM system performance might be reduced but should remain at an acceptable level until the sensors can be repaired or replaced. It is essential to assess the influence of sensor loss on damage detection capability. The most critical sensor loss is defined as the sensor failure that leads to the most dramatic coverage reduction in the critical damage location.

5

Level 3: Quantification of damage localisation capability. If the acceptable detection performance of critical damage is achieved in level 2, damage localisation performance is quantified at level 3. Two approaches to quantify localisation capability are proposed. The first approach considers a number of localization estimates of the critical defects and quantifies the trueness (how close is the average estimation to the true location) and precision (the deviation among the estimations). Another approach is to quantify the localisation performance by providing reliability measure of the localization estimates in various critical areas of the structure, i.e. the true location of the defect is in a certain area given the estimation is in this area, which is achieved with Gaussian Kernel distribution estimation and Bayesian inference.

The methodologies used in each level of quantification are presented in the following subsections.

2.1. Level 0: Optimal sensor placement

Given a CFRP airframe structure and its critical impact scenarios, a guided wave SHM system can be designed to identify impact damage while maintain a reasonable cost. The amount of sensor implemented is a prime factor to GWSHM system implementation and in-service costs, and its a key constrain to GWSHM system design.

Thiene at al.[24] proposed a sensor placement method to achieve the maximum area coverage with a fixed number of piezoelectric sensors. A fitness function was introduced as an indicative measure of damage detection capability of a sensor network placement. A genetic algorithm (GA) is applied to find the optimal sensor placement based on the fitness function. This method is adopted in level 0 and is introduced as follows.

The fitness function of sensor placement considers geometrical constraints and physical constraints.

Geometrical constraints include:

i) the detectability distribution of a sensor pair by adding value 1 ($flag(pix, path) = flag(pix, path) + 1$) in on the direct sight of a sensor pair and 0 ($flag(pix, path) = flag(pix, path)$) elsewhere, as demonstrated in Figure 2a. This is optional depending on whether the detection and/or localisation algorithm favours the direction path.
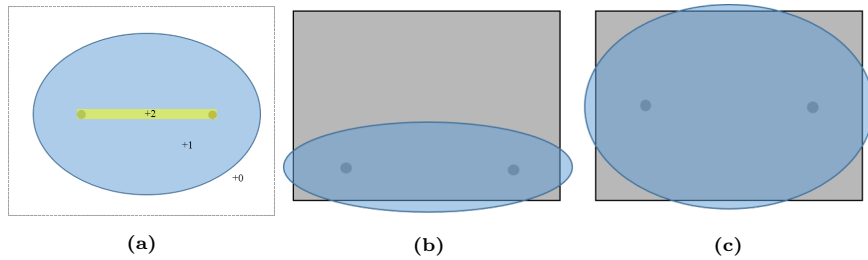

(a)   (b)   (c)

Figure 2: Effective coverage area of a sensor pair (a) with added coverage value on the direct sight, (b) close to the boundary of the panel and (c) far from the boundary of the panel.

ii) minimising boundary reflections. In order to determine if a transducer pair should have a positive contribution to the overall fitness function, a threshold ξ is defined for the proportion of the ellipse perimeter inside the boundaries:

$$flag(pix, path) = \begin{cases} flag(pix, path) + 1 & \text{if } l_{ins} \geq \xi l_{tot}, \\ flag(pix, path) & l_{ins} < \xi l_{tot}. \end{cases} \tag{1}$$

Boundary reflection coefficient ξ is tuned by the user depending on how well the boundary reflection is dealt with in the chosen damage detection and/or localisation algorithm. Figure 2(b)(c) shows the elliptical area of a sensor pair with boundary threshold ξ set to 0.75.

iii) disruption of guided wave propagation path by openings. Wave propagation would be interrupted and the incident wave cannot be evaluated based on the direction distance between the transducers and the pixel if opening presents in any of the following positions, as shown in Figure 3.
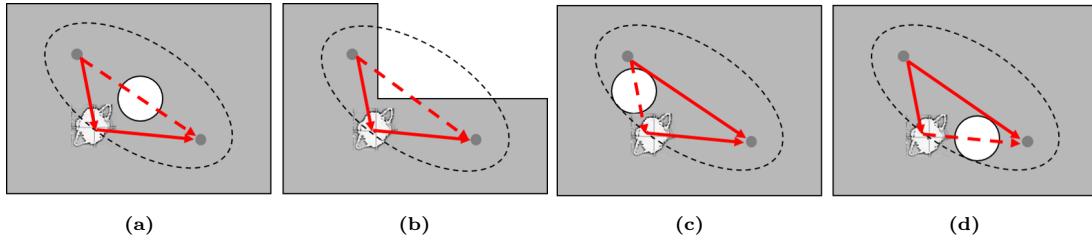

Figure 3: Disruption of wave propagation by openings: direct path between (a) actuator or (b) sensor; (c) path between the actuator and pixel; (d) path between the pixel and the sensor.

The global coverage of the sensor network is obtained by summing the values produced by each transducer pair as:

$$cov(pix) = \sum_{pair} flag(pix, pair) \tag{2}$$

The physical constraints of the fitness function of sensor placement lies within the guided wave attenuation and frequency. It is known that the attenuation of guided waves is dependent on the excitation frequency. It is also assumed that the minimum detectable damage size is related to the excitation frequency though the wavelength of the guided wave. Therefore, the physical constraints are expressed as the frequency factor ζ_f which is assigned to each actuator-sensor pair for a particular pixel:

$$\zeta_f = A * \exp(B * distance) \tag{3}$$

where A and B are the two coefficients of the exponential trendline related to the selected actuation frequency.

The fitness function is determined by fusing the values from all the transducer paths and summing for all the pixels, to obtain a single coefficient as:

$$c = \sum_{pix} cov(pix) \cdot \zeta_f \tag{4}$$

It is assumed that the best performance of the transducers network is reached when the fitness function is maximised.

2.2. Level 1: Quantification of noise under environmental and operational conditions

Novelty detection has been a popular unsupervised approach for machine condition monitoring and used by a number of authors in guided wave based structural damage detection, as only data from healthy or pristine structures are required to establish damage detection criteria[25][26][27][28][29]. Novelty detection approaches generally involve extracting damage sensitive features, establishing damage indices via feature fusion and threshold setting.

As GWSHM system is designed to be operating on the structure without major disruption of aircraft service, guided wave measurements are likely to be recorded on a operating aircraft in varying environmental and operational conditions, and hence contain a significant level of noise that might greatly comprise the damage detection performance. It is a crucial step to quantify the uncertainty of damage sensitive features in a pristine structure under the designed environmental and operational conditions for threshold setting in order to achieve reliable damage detection.

In this work, damage detection is considered as a novelty detection problem. The damage sensitive features from sensor pairs are extracted and fused according to the sensor coverage distribution. The global distribution of fused features is used as a global damage index and its threshold is derived from the noise level in damage sensitive features under pristine condition.

Sensor coverage. A key aspect to be considered in establishing a global damage index is the guided wave coverage area. To achieve reliable guided wave inspection of a large and complicated structure, a dense sensor network is usually implemented in order to cover the structure with effective diagnostic guided waves from multiple propagation directions in order to increase the change of capturing damage. A large number of the damage sensitive features are obtained from the dense sensor network and they contain common information due to the overlapping guided wave propagating region. The fusion of the damage sensitive features should consequently consider guided wave coverage distribution.

Having determined the optimal sensor placement in level 0, the corresponding sensor coverage on the target structure can be obtained using equation (2). Figure 4 shows the sensor coverage in a simple flat panel with an eight-sensor network.
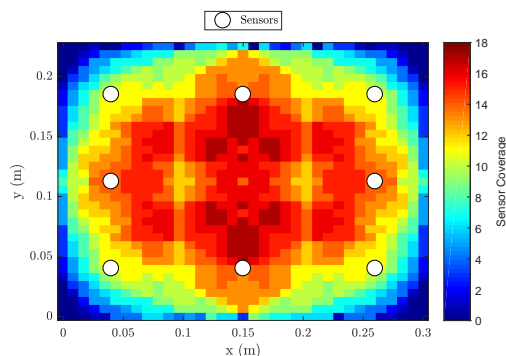

Figure 4: Sensor coverage of an eight-sensor network.

Sensor coverage is an indicative measurement of the probability of capturing damage, i.e. the more effective guided wave paths available at a location, the more likely damage at this location can be captured. However, this is under the assumption that guided waves are only affected by the occurrence of damage. In a real application scenario, guided wave signals are likely to be acquired in various environmental and operational conditions. The difference in a current signal and a baseline signal is no longer only caused by the occurrence of damage, but also by a difference in the measurement condition. In this case, sensor coverage is not sufficient to describe the damage detection capability of a sensor network. The variation in damage sensitive signal features in the intended environmental and operational conditions must be quantified in order to achieve reliable damage detection.

Damage-sensitive signal feature. Guided waves are dispersive in nature, but for a certain frequency and plate thickness, the two fundamental guided wave modes, A0 and S0, are nearly non-dispersive. The non-dispersive guided wave response is achieved by frequency selection. Signal response to tone-burst signals at selected frequencies are recorded for a sensor network under the pre-defined environmental and operational conditions. Denoting the mth recoding of the signal with sensor pair i as $s_{im}(t)$. The effective signal, $s_{im}^{w}(t)$, containing an acceptable amount of boundary reflected wave can be obtained according to equation (2.2)

$$s_{im}^{w}(t) = s_{im}(t)W_i(t) \qquad (5)$$

where $W_i(t)$ is the damage sensitive time window function defined as:

$$W_i(t) = \begin{cases} 1 & \text{if } \tau_i^a < t < \tau_i^b, \\ 0 & \text{otherwise.} \end{cases} \qquad (6)$$

where τ_i^a is the time of flight of a guided wave from the actuator to the sensor via the shortest path, calculated as:

$$\tau_i^a = \frac{d_{A-S}}{v} \qquad (7)$$

8

where d_{A-S} is the distance between the actuator and the sensor, v is wave velocity. τ_i^b is the time of flight of wave guide from the actuator passing the edge of the largest effective elliptical area (as shown in Figure 2) then to the sensor, calculated as:

$$\tau_i^b = \frac{d_{A-E}}{v} + \frac{d_{E-S}}{v} \tag{8}$$

where d_{A-E} and d_{E-S} are the distance from the actuator and the sensor to a point on the edge of the largest effective elliptical area, respectively.

Let $u_{im}(t)$ refer to the residual signal between the current signal of interest, $s_{im}^w(t)$, and the reference signal, $s_i^{ref,w}(n)$,

$$u_{im}(t) = s_{im}^w(t) - s_i^{ref,w}(t) \tag{9}$$

The magnitude of the residual signal is obtained using Hilbert transform as:

$$u_{im}^e(t) = |u_{im}(t) + iH[u_{im}(t)]| \tag{10}$$

$H[\cdot]$ denotes the Hilbert transform. r_{im} denote the peak value of the residual envelop:

$$r_{im} = \max u_{im}^e(t) \tag{11}$$

The time position of the peak residual envelop is:

$$\tau_{im} = \operatorname*{argmax}_{t} u_{im}^e(t) \tag{12}$$

Assume r_{im} follows a normal distribution. It can be described as a Gaussian random variable R_i with mean $\hat{\mu}_i$ and variance $\hat{\sigma}_i^2$. Maximum likelihood estimations of $\hat{\mu}_i$ and $\hat{\sigma}_i^2$ from M samples $(r_{i1}, ..., r_{im}, ..., r_{iM})$ are:

$$\hat{\mu}_i = \bar{r}_i = \frac{1}{M} \sum_{m=1}^{M} r_{im} \tag{13}$$

$$\hat{\sigma}_i^2 = \frac{1}{M-1} \sum_{m=1}^{M} (r_{im} - \bar{r}_i)^2 \tag{14}$$
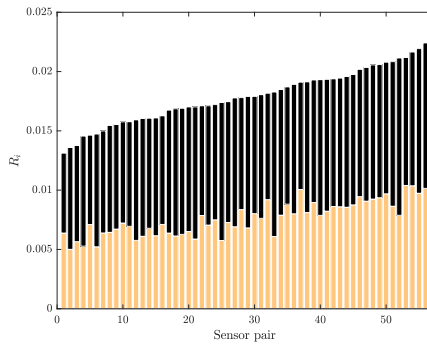

Figure 5: The upper bound of 56 damage-sensitive features in pristine state. The yellow bar represents the value of $\hat{\mu}_i$ and the black bar indicates the value of $Z_{99.9\%}\hat{\sigma}_j$. The sensor pairs are sorted by their upper confidence bound value.

Feature fusion and threshold setting. Two feature fusion and threshold setting methods are presented and discussed here: (1) Sensor pairwise based damage detection and (2) Spatial damage indices based damage detection.

Sensor pairwise based damage detection. Sensor pairwise detection is the simplest approach and is commonly adopted in the literature[29][30][7], especially for one pair of sensors. The damage-sensitive features from each individual sensor pair are used to create an damage index for that sensor pair. As the mean and standard deviation of the damage-sensitive features in pristine state are known from equations (13) and (14), the upper bound of the feature value from sensor pair i in pristine state can be calculated and serves as the damage detection threshold Th_i for this sensor pair:

$$Th_i = \hat{\mu}_i + Z_{99.9\%}\hat{\sigma}_j \tag{15}$$

where $Z_{99.9\%}$ is the Z-score corresponding to 99.9% confidence. Figure 5 presents the derived thresholds for 56 damage sensitive features obtained from every sensor pair in a sensor network of 8.

However, in large and complex structures, a large network of sensors are required for adequate damage detection capability and high sensor coverage for critical locations. A drawback of sensor pairwise detection is that it might result in ambiguous global damage detection result due to inconsistent damage indication from different sensor paths. This approach also ignores information regarding the spatial position of sensor pairs and their common coverage area. This is particularly important in a dense sensor network.

Spatial damage indices based damage detection. A damage detection strategy that considers spatial sensor placement is proposed. The damage sensitive features from all sensor pairs in the sensor network are fused according to the coverage area to derive spatially distributed damage indices. A global damage index is then determined based on the global feature of the spatial damage damage indices. A threshold of the global damage index for damage detection can be determined according to the variability of the global damage index when no damage is present.

(1) Sensor network coverage based feature fusion. The damage-sensitive features extracted from all signal paths are fused according to the sensor coverage to derive a damage index based on the spatial distribution of the sensors.

To fuse signal features based on sensor network coverage, the structure is partitioned into J pixels and the assigned value to each pixel is included in the spatial damage index vector $\mathbf{I}$, $\mathbf{I} = [I_1, ..., I_j, .., I_J]$. The sensor pairs whose coverage area contains the pixel j contribute to I_j. Denoting those sensor pairs as k, $k = 1, 2, ..., n_j$, where n_j is the number of effective sensor pairs available at pixel j.

$$I_j = \frac{\sum_{k=1}^{n_j} R_k}{n_j} \tag{16}$$

where R_k is a Gaussian random variable with mean $\hat{\mu}_k$ and standard deviation $\hat{\sigma}_k$, $\hat{\mu}_k$ and $\hat{\sigma}_k^2$ are calculated from equations (13) and (14). As the signals recorded via different sensor pairs are independent, I_j is normally distributed with mean $\hat{\mu}_j$ and variance $\hat{\sigma}_j^2$,

$$\hat{\mu}_j = \frac{\sum_{k=1}^{n_j} \hat{\mu}_k}{n_j} \tag{17}$$

$$\hat{\sigma}_j^2 = \frac{\sum_{k=1}^{n_j} \hat{\sigma}_k^2}{n_j^2} \tag{18}$$

When signal features are averaged as in equation (18) at their mutual pixel location, the variance of the averaged signal features are reduced.
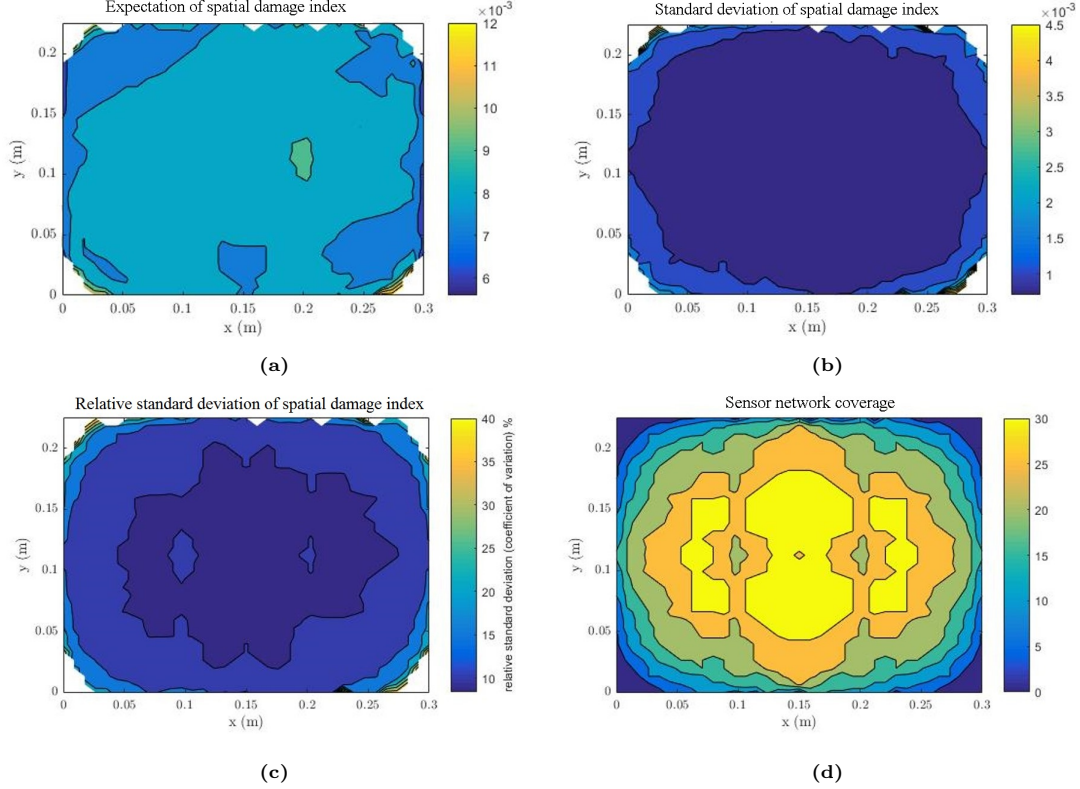
Figure 6: Spatial distribution of (a) expectation of the spatial damage index **I**, $\hat{\mu}_j$, (b) standard deviation of the spatial damage index **I**, $\hat{\sigma}_j$, (c) relative standard deviation $\hat{\sigma}_j/\hat{\mu}_j$ and (d) sensor network coverage.

Spatial distribution of the expected value of spatial damage index $\hat{\mu}_j$ and the standard deviation of spatial damage index $\hat{\sigma}_j$ of an eight-sensor network are presented in Figures 6(a) and (b), respectively. In order to reflect the uncertainty of spatial distributed damage indices, the relative standard deviation, $\hat{\sigma}_j/\hat{\mu}_j$, is presented in Figure 6(c). It can be seen that the distribution of relative standard deviation has similarity to the sensor network coverage distribution shown in Figure 6(d). The positions with high sensor coverage have low relative standard deviation of the spatial damage index. According to equation (18), as sensor coverage increases, the standard deviation of the spatial damage index reduces, i.e. uncertainty of the spatial damage index reduces.

(2) Threshold setting. To decide whether damage is present in the structure, a detection criteria is established for the spatially distributed damage index considering the uncertainty from a range of pre-defined environmental and operational conditions.

Let d and $\hat{d}$ denote the actual and the estimated integrity state of the structure, respectively. Both d and $\hat{d}$ are binary values with 0 signifying 'pristine' and 1 signifying 'damaged', respectively.

If the spatial damage indices of an unknown state deviate from the value range at the pristine state with variation caused by varying environmental and operational conditions, it is considered that the damage is present in the structure.

The spatial damage index value represents the likelihood of damage presence at the spatial location. A spatial damage index value at the pristine state is $I_j|(d=0)$. Its mean $\hat{\mu}_j|(d=0)$ and standard deviation $\hat{\sigma}_j|(d=0)$ are calculated from equations (17) and (18), respectively. The 'normal' value range of $I_j|(d=0)$ is considered to be less than its 99.9% upper confidence bound. This is calculated as:

$$I_{j99.9\%}|(d=0) = \hat{\mu}_j|(d=0) + Z_{99.9\%}\hat{\sigma}_j|(d=0) \tag{19}$$

where $Z_{99.9\%}$ is the z-score corresponding to 99.9% confidence, $\hat{\mu}_j|(d=0)$ and $\hat{\sigma}_j|(d=0)$ are calculated in equations (17) and (18).

For damage detection within a designed sensor coverage area, the global value of the spatial damage index vector $\mathbf{I}$ is considered. In the conventional ROC approach, the threshold is swept over the range of feature values [16], which does not provide a practical way of threshold setting. Here, the detection threshold is set at a percentile position of the spatial damage index vector $\mathbf{I}_{99.9\%}|(d=0)$, denoted as the global damage index (GDI).

As an intuitive attempt, a threshold γ is set at the 50th percentile of $I_{99.9\%}|(d=0)$, indicating that 50% of the spatial damage indices are below this threshold with no less than 99.9% confidence. Figure 7(a) shows the spatial damage indices of a sensor network where the spatial damage indices are sorted by their 99.9% upper confidence bound. The threshold γ is set at the 80th percentile of the spatial damage indices.
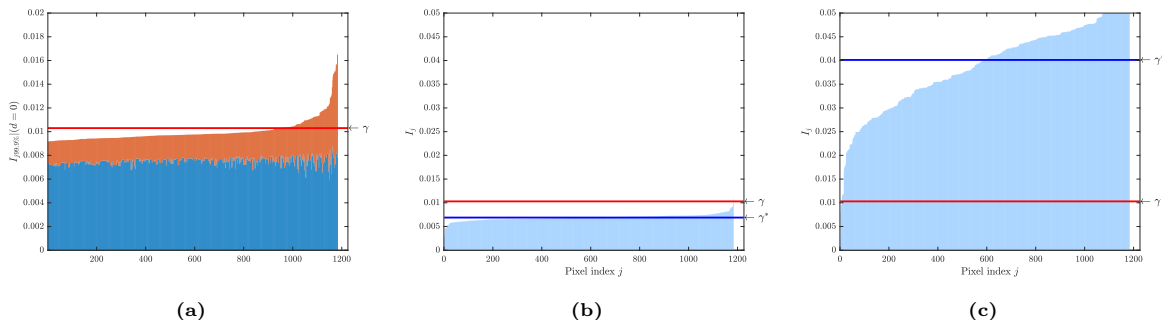
Figure 7: Damage detection criteria. (a) Threshold setting for damage detection. The orange bars indicate $\hat{\mu}_j|(d=0)$, the blue bars represent the confidence range considering uncertainty $Z_{99.9\%}\hat{\sigma}_j|(d=0)$. The threshold γ is set at 80th percentile of the damage indices. (b) negative result as $\gamma^* < \gamma$, $\hat{d}=0$ and (c) positive result, $\gamma^* > \gamma$, $\hat{d}=1$.

For a structure whose integrity state is known, its spatial damage index vector, denote as $\mathbf{I}|(d=?)$, is obtained using equation (16) with R_k denoting the current signal feature value. The global damage index is set at the 50th percentile of the spatial damage index vector, denote as γ^*. The γ^* value at the damaged state is assumed to be larger than at the pristine state. Thus if $\gamma^* > \gamma$, meaning 50% of the spatial damage indices are higher than the threshold, the damage detection result is positive, $\hat{d}=1$, as shown in Figure 7(c). Otherwise the damage detection result is negative, $\hat{d}=0$, as shown in Figure 7(b).

2.3. Level 2: Quantification of damage detection capability

Illustrative model for damage detection. An illustrative damage model is developed to demonstrate the damage detection process and highlight the influential factors. The model considers damage located at a certain position on the target structure. The size of the damage is neglected for simplicity. It is assumed that the damage sensitive features of a signal increase to a certain level if sensor coverage area contains the assumed damage position.

Assume damage occurs at a location, denote all signal features by $*$. Let R_i^* represent the current damage-sensitive features obtained from the sensor pair i. Denote $R_i^*|(d=1)$ if the sensor pair has effective coverage at the damage location, otherwise denote $R_i^*|(d=0)$. The mean values of $R_i^*|(d=1)$ are increased to μ^* and the mean values of $R_i^*|(d=0)$ remains $\hat{\mu}_i$. Assume the standard deviation of R_i^* remain the same, thus $\hat{\sigma}_i^2$ still applies, we have

$$
\begin{aligned}
R_i^*|(d=1) &\sim N(\mu^*, \hat{\sigma}_i^2) \\
R_i^*|(d=0) &\sim N(\hat{\mu}_i, \hat{\sigma}_i^2)
\end{aligned}
\tag{20}
$$

The spatial damage index $\boldsymbol{I}^*|(d=1)$ is derived by calculating the mean and variance of the spatial damage index from equations (17) and (18). The global damage index, γ^*, is obtained as the 50th percentile of the spatial damage index vector.
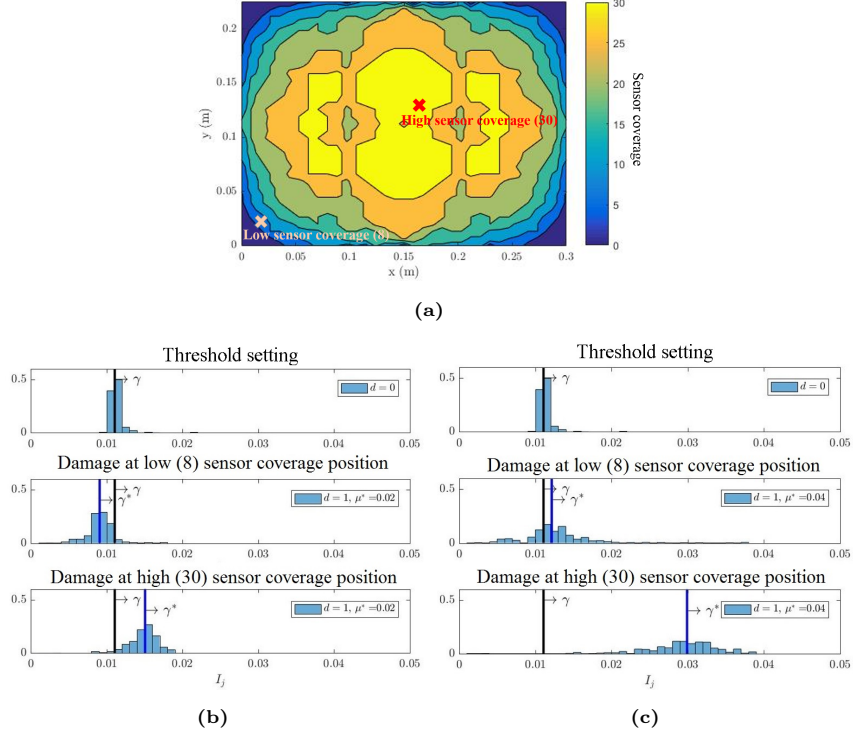
Figure 8: Demonstration of damage detection with an illustrative model. (a) Sensor coverage distribution of the sensor network. The red cross marks the damage location at high (30) sensor coverage position, the pink cross marks the damage location at low (8) sensor coverage position. (b) Low damage severity. (c) High damage severity.

Figure 8 presents the distribution of the spatial damage index value obtained with the model. Two damage severity levels are considered by assuming the damage-sensitive signal feature to increase to 0.02 and 0.04, presented in Figures 8(b) and (c), respectively. For each damage severity, damage at a low sensor coverage position and a high sensor coverage position are considered. It can be seen that damage at positions with high sensor coverage results in greater global damage index, thus the damage is more likely to be detected ($\gamma^* > \gamma$). If the damage has a low severity and is located at a low sensor coverage position, it might not be detected ($\gamma^* < \gamma$). To improve the probability of detecting damage at a certain position, the sensor coverage at this position should be made sufficient, and the minimum detectable size of the damage should be carefully determined.

Alternative detection sensitivity can be achieved by evaluating different values of the threshold γ and the global damage index γ^*. Different values of γ can be estimated by varying the Z value representing the confidence level in equation (19) as well as altering the percentile positions of the upper confidence bound for the pristine spatial damage index vector at which the γ value is adopted. Different values of the global damage index γ^* can be estimated by adopting different percentile positions of the spatial damage index vector as the global damage index.

Redundancy of a sensor network. As demonstrated in Figure 8, good sensor coverage is critical for damage detection under the presence of uncertainties. As degradation or failure of sensors is unavoidable during long term monitoring, a redundant design concept must be adopted for the reliable long-term service of a GWSHM system, i.e. the sensor coverage in critical locations on the structure must be redundant.

The redundancy of a sensor network can be assessed by the sensor coverage under critical sensor loss. Critical sensor loss is determined as the sensor failure that leads to the most dramatic coverage reduction at the critical damage location. When critical sensor loss occurs, the sensor network coverage should still be sufficient for the target structure. Examples of redundant sensor network design are presented in Figure 9.
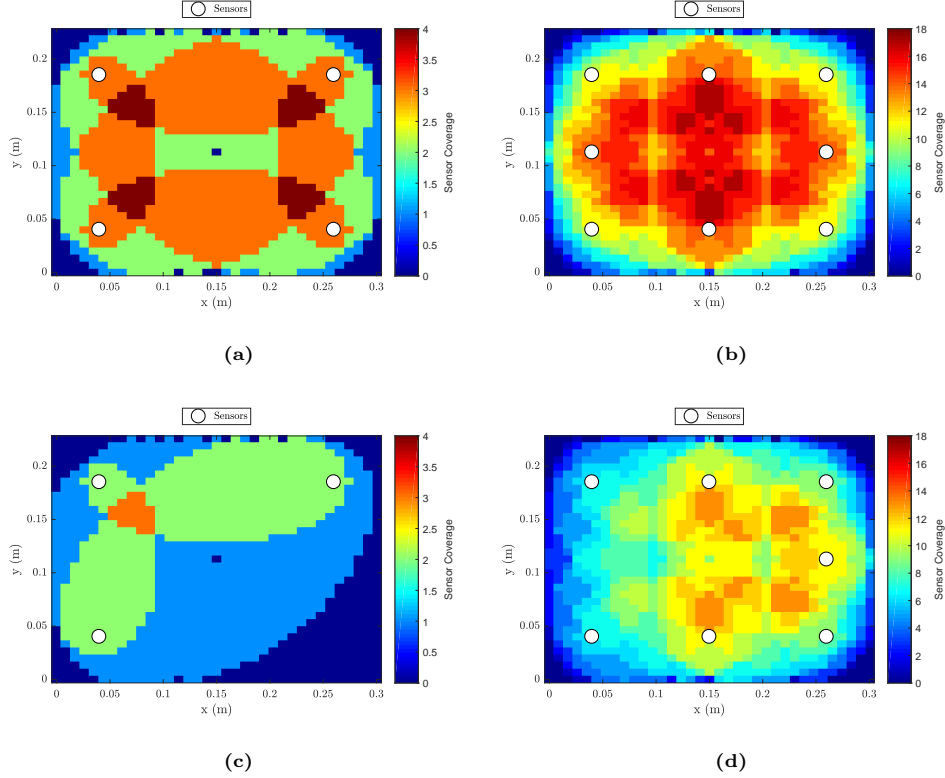
Figure 9: Sensor coverage of (a) four sensors, (b) eight sensors, (c) three sensors and (d) seven sensors

Four-sensor network and eight-sensor network are two possible sensor network placements, as shown in Figures 9(a) and (b), respectively. Assuming one sensor is faulty and thus eliminated from the sensor network, the coverage of the four-sensor network is reduced from 3 to 0 near the faulty sensor location, as shown in Figure 9(c), which is not acceptable. The eight-sensor network, however, only suffer from coverage drop from 14 to 6 at the faulty sensor location, as shown in Figure 9(d), which is still sufficient for damage detection. Therefore, the eight-sensor network is considered more robust than the four-sensor network.

Detection performance evaluation. As discussed in the introduction, hit/miss analysis is used for the reliability assessment in detecting BVID. Table 1 presents the four outcomes of damage detection.

Table 1: Detection outcomes

		True state	
		$d = 0$	$d = 1$
Predicted state	$\hat{d} = 0$	True negative (TN)	False negative (FN)
	$\hat{d} = 1$	False positive (FP)	True positive (TP)

Probability of detection (POD), $p(\hat{d} = 1 | d = 1)$, and probability of false alarm (PFA), $p(\hat{d} = 1 | d = 0)$, are calculated as

$$POD = p(\hat{d} = 1 | d = 1) = \frac{\text{TP}}{\text{TP+FP}}$$
$$PFA = p(\hat{d} = 1 | d = 0) = \frac{\text{FP}}{\text{TN+FP}} \tag{21}$$

The ratio of correct predictions to the total number of predictions made, $p(\hat{d} = d)$, is defined as accuracy:

$$Accuracy = p(\hat{d} = d) = \frac{\text{TP + TN}}{\text{TP + TN + FP + FN}} \tag{22}$$

14

2.4. Level 3: Quantification of damage localisation capability

As a result of level 2, the damage detection capability of a sensor network in the pre-defined environmental and operational conditions is quantified. For large scale structures with critical positions where damage can significantly reduce the residual life of the structure, the location of the damage provides important information for complimentary localised non-destructive inspection and maintenance actions. Therefore, in level 3, approaches to quantify damage localisation capability are proposed.

In this work, a commonly used imaging method in the literature, Delay-and-Sum (DAS), is used for damage localisation. Other damage imagining methods can be applied and assessed in a similar manner.

DAS method is well documented in a number of publications. For the completeness of this work, a brief description is given here. In the DAS method, the envelop of residual signals from each sensor pair, $e_n(t)$, are "delayed" by the calculated wave propagation time of a point $\boldsymbol{x}$ within the region of interest and summed for the spatial likelihood index [31]:

$$L(\boldsymbol{x}) = \frac{1}{N} \sum_{n=1}^{N} e_n[\tau_n(\boldsymbol{x})] \tag{23}$$

where $\tau_n(\boldsymbol{x})$ is the corresponding time of arrival calculated for pixel location $\boldsymbol{x}$.

Guided wave velocity is used to calculate the expected arrival time of scattered signal. The time delay is calculated as

$$\tau_n(\boldsymbol{x}) = \frac{d_n^a(\boldsymbol{x})}{V_a} + \frac{d_n^s(\boldsymbol{x})}{V_s} + t_{\text{off}} \tag{24}$$

where V_a is wave velocity in the direction from the actuating transducer to the location $\boldsymbol{x}$ and V_s is wave velocity in the direction from the location $\boldsymbol{x}$ to the sensing transducer. t_{off} is time lag accounting for delays in acquisition system.

The spatial likelihood index is transformed to dB scale as $10 \log_{10} L(\boldsymbol{x})$ and the damage location estimate is determined as

$$\hat{\boldsymbol{x}} = \underset{\boldsymbol{x}}{\operatorname{argmin}} \, 10 \log_{10} L(\boldsymbol{x}) \tag{25}$$

In order to suppress the effect of noise in the damage imaging process and damage location estimation, a two step noise-suppressing technique is proposed:

(1) A mean filter. Mean filter is used to suppress the sparse extreme values in the spatial likelihood indices which are unlikely to be the damage location. The spatial likelihood index $L(\boldsymbol{x})$ is updated by the average value of its nearest rectangular neighbourhood of over 7×7 pixels neighbourhood (5cm × 4cm area). Figure 10 represents the spatial likelihood index distribution derived from DAS before and after mean filtering.
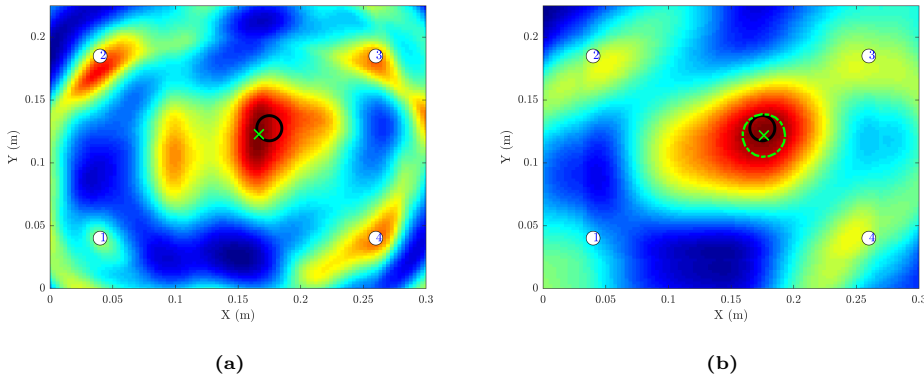

(a)   (b)

Figure 10: Application of a mean filter on the spatial likelihood index $L(\boldsymbol{x})$. $L(\boldsymbol{x})$ derived from DAS (a) before mean filtering and (b) after mean filtering. The black circle indicates the actual damage location. The green circle marks the estimated damage location.

15

(2) Determine location estimate. The estimated damage location is usually determined at the location where the the spatial likelihood index is the greatest. However, as the spatial likelihood index might be corrupted by noise and the maximum spatial likelihood location for the same damage may vary significantly, causing low precision in the location estimate. In order to eliminate the effect of noise, the damage location is estimated based on a group of possible location estimates.

Instead of taking the location estimate at which the spatial likelihood indices are the maximum, the locations whose spatial likelihood indices are among the top 1% are selected as possible locations with equal likelihood to be the actual damage. These locations are then represented by the smallest enclosing circle, and the centre of this circle is taken the estimated damage location, as shown in Figure 10(b).

Localisation performance evaluation approaches. The purposes of evaluating the damage localisation method are:

- To quantify the accuracy of the location estimates obtained from a certain localisation method.

- To provide practical guidance/reference for future maintenance decisions.

Two approaches are proposed accordingly to quantify the performance of the selected localisation method. The first approach is to quantify the accuracy of the location estimate of damage in a certain critical area on the structure. The second approach considers the damage locations in various zones on the target structure and uses statistical methods to derive the probability of correctly indicating damage in certain zones.

The two approaches are introduced as follows:

(1) Accuracy of location estimation of damage in critical locations. According to BS ISO 5725-1: Accuracy of measurement methods and results [32, 33], the accuracy of a measurement method can be quantified in terms of trueness and precision: "Trueness is the closeness of the mean of a set of measurement results to the actual (true) value and precision is the closeness of agreement among a set of results". Two types of errors are normally present in a measurement process: random error and systematic error. Random error is caused by random noise and an unbiased simplification of the process. Systematic error is the result of incomprehensible modelling assumptions and inappropriate simplification. Precision is impaired by random error while trueness is undermined by systematic error.

The trueness of the location estimate is calculated from a number of location estimates $\hat{\boldsymbol{x}}(\hat{x}_m, \hat{y}_m)$. Trueness is measured as the Euclidean distance between the arithmetic mean of the location estimates and the actual location $\boldsymbol{x}_d$ (x_d, y_d).

$$\bar{x} = \frac{\sum_{m=1}^{M} \hat{x}_m}{M}, \bar{y} = \frac{\sum_{m=1}^{M} \hat{y}_m}{M} \tag{26}$$
$$Trueness : \sqrt{(\bar{x} - x_d)^2 + (\bar{y} - y_d)^2}$$

The precision of the location estimate is calculated as the area of the ellipse representing the covariance matrix. The steps to derive precision are:

(a) Obtain the covariance matrix of $\hat{\boldsymbol{x}}$, find the two eigenvectors in the largest and smallest variance direction

(b) Find largest and smallest eigenvalues: largest variance a^2 and smallest variance b^2

(c) Determine the enclosing ellipse with 95% confidence level: find the critical value of chi-square distribution corresponding to 95% confidence level with 2 degree freedom, note as $\chi^2_{2,95\%}$. The equation of the ellipse can then be written as:

$$\frac{(x - \bar{x})^2}{a^2} + \frac{(y - \bar{y})^2}{b^2} = \chi^2_{2,95\%} \tag{27}$$

(d) The precision of location estimate is measured as the enclosing area of the ellipse:

$$Precision : \pi ab\sqrt{\chi^2_{2,95\%}}. \tag{28}$$

(2) Probability of correctly indicating a defect within a certain zone. For structures with added complexity such as stiffeners and openings, the mechanical performance of the structure might be significantly impaired by defects at certain locations such as the foot of stiffener or corner of an opening. Accurate localisation of defects in these locations is crucial to condition-based maintenance of such structures as they represent the worst case scenario.

A two step approach for estimating the probability of correctly indicating defects within a certain zone is proposed. The first step is to derive the density distribution of the location estimates for a defect at various zones of the structure using Gaussian kernel density function estimation. The second step is to calculate the probability that the actual defect is in a certain zone when the location estimation falls inside this zone using Bayes' law.

The approach is presented as follows:

(a) Probability density distribution of the location estimates [21]. The target structure is partitioned into a grid of positions $\boldsymbol{x}(x,y)$. The probability density function of estimated damage locations, $\hat{\boldsymbol{x}}_m(\hat{x}_m, \hat{y}_m)$, when the actual damage is located at $\boldsymbol{x}_d(x_d, y_d)$, is estimated using Gaussian kernel:

$$\hat{f}_h(\boldsymbol{x}|\boldsymbol{x}_d) = \frac{1}{M^{(d)}h} \sum_{m=1}^{M^{(d)}} \frac{1}{\sqrt{2\pi}} \exp[-\frac{|\hat{\boldsymbol{x}}_m - \boldsymbol{x}|^2}{2h^2}] \tag{29}$$

where h is kernel bandwidth.

(b) Probability of correctly indicating damage in a critical zone. Divide the plate into critical zone C and non critical zone $\bar{C}$. The critical zone C can be defined based on the sensor network coverage or the locations where a defect is expected to significantly reduce the mechanical performance of the target structure.

Two localisation results are the location estimation falls within the critical zone, $E_1 : \hat{\boldsymbol{x}} \in C$, and when it falls outside the critical zone, $E_2 : \hat{\boldsymbol{x}} \in \bar{C}$. Two hypotheses about the actual damage location regarding the critical zone can be made, the actual damage location is in the critical zone, $H_1 : \boldsymbol{x}_d \in C$, and is not in the critical zone $H_2 : \boldsymbol{x}_d \in \bar{C}$.

Prior probabilities of H_1 or H_2 are dependent on the probability of damage occurrence in zone C and $\bar{C}$, respectively. Consider uniform probability of damage occurrence, the prior probability can be calculated as the area ratio:

$$P(H_1) = \frac{area(C)}{area(C) + area(\bar{C})}$$
$$P(H_2) = \frac{area(\bar{C})}{area(C) + area(\bar{C})} \tag{30}$$

The posterior probability that the actual damage location is in zone C when the location estimation falls in zone C is:

$$p(H_1|E_1) = \frac{p(E_1|H_1)P(H_1)}{p(E_1|H_1)P(H_1) + p(E_1|H_2)P(H_2)} \tag{31}$$

where likelihood $p(E_1|H_1)$ and $p(E_1|H_2)$ are estimated using density estimation obtained from equation (29). The probability $p(E_1|H_1)$ is calculated with all available $\{\boldsymbol{x}_d|\boldsymbol{x}_d \in C\}$:

$$p(E_1|H_1) = p(\hat{\boldsymbol{x}} \in C|\boldsymbol{x}_d \in C) = \frac{\int_{\boldsymbol{x} \in C} \hat{f}_h(\boldsymbol{x}|\boldsymbol{x}_d \in C)d\boldsymbol{x}}{\int_{\boldsymbol{x}} \hat{f}_h(\boldsymbol{x}|\boldsymbol{x}_d \in C)d\boldsymbol{x}} \tag{32}$$

and $p(E_1|H_2)$ is calculated with all available $\{\boldsymbol{x}_d|\boldsymbol{x}_d \in \bar{C}\}$:

$$p(E_1|H_2) = p(\hat{\boldsymbol{x}} \in C|\boldsymbol{x}_d \in \bar{C}) = \frac{\int_{\boldsymbol{x} \in C} \hat{f}_h(\boldsymbol{x}|\boldsymbol{x}_d \in \bar{C})d\boldsymbol{x}}{\int_{\boldsymbol{x}} \hat{f}_h(\boldsymbol{x}|\boldsymbol{x}_d \in \bar{C})d\boldsymbol{x}} \tag{33}$$

Likewise, the posterior probability of actual damage is in zone $\bar{C}$ when the estimation falls in zone $\bar{C}$ is given as:

$$p(H_2|E_2) = \frac{p(E_2|H_2)P(H_2)}{p(E_2|H_1)P(H_1) + p(E_2|H_2)P(H_2)} \tag{34}$$

where

$$p(E_2|H_1) = p(\hat{\boldsymbol{x}} \in \bar{C}|\boldsymbol{x}_d \in C) = \frac{\int_{\boldsymbol{x} \in \bar{C}} \hat{f}_h(\boldsymbol{x}|\boldsymbol{x}_d \in C)d\boldsymbol{x}}{\int_{\boldsymbol{x}} \hat{f}_h(\boldsymbol{x}|\boldsymbol{x}_d \in C)d\boldsymbol{x}} \tag{35}$$

and

$$p(E_2|H_2) = p(\hat{\boldsymbol{x}} \in \bar{C}|\boldsymbol{x}_d \in \bar{C}) = \frac{\int_{\boldsymbol{x} \in \bar{C}} \hat{f}_h(\boldsymbol{x}|\boldsymbol{x}_d \in \bar{C})d\boldsymbol{x}}{\int_{\boldsymbol{x}} \hat{f}_h(\boldsymbol{x}|\boldsymbol{x}_d \in \bar{C})d\boldsymbol{x}} \tag{36}$$

The approach above can also be expended for N zones on the structure, $C_n, n = 1, ..., N$. The corresponding events are $E_n : \hat{\boldsymbol{x}} \in C_n, n = 1, ..., N$. The corresponding hypothesis are $H_n : \boldsymbol{x}_d \in C_n, n = 1, ..., N$. The probability that damage is located in zone C_n when a location estimate falls within zone C_n is calculated as:

$$p(H_n|E_n) = \frac{p(E_n|H_n)P(H_n)}{\sum_{n=1}^{N} p(E_n|H_n)P(H_n)} \tag{37}$$

where

$$p(E_m|H_n) = p(\hat{\boldsymbol{x}} \in C_m|\boldsymbol{x}_d \in C_n) = \frac{\int_{\boldsymbol{x} \in C_m} \hat{f}_h(\boldsymbol{x}|\boldsymbol{x}_d \in C_n)d\boldsymbol{x}}{\int_{\boldsymbol{x}} \hat{f}_h(\boldsymbol{x}|\boldsymbol{x}_d \in C_n)d\boldsymbol{x}} \tag{38}$$

and prior probability of hypothesis H_n is given by the probability of damage occurrence, $f(x_d \in C_n)$:

$$p(H_n) = \frac{\int_{x_d \in C_n} f(x_d)dx_d}{\int_{x_d} f(x_d)dx_d} \tag{39}$$

In the case of uniformly distributed damage occurrence, $p(H_n)$ is the area fraction of zone C_n

$$p(H_n) = \frac{area(C_n)}{\sum_{n=1}^{N} area(C_n)} \tag{40}$$

3. Quantification of GWSHM on CFRP coupons

This section presents the quantification process of GWSHM on CFRP coupons up to size 500 mm $\times$250 mm in temperature controlled laboratory conditions. Temperature compensation of guided wave measurements was not necessary As the temperature variation was small (within 2°C). Temperature compensation method can be implemented for airframe structures in the case of greater temperature variation[6].

Simple flat panels (300 mm $\times$225 mm) made from three types of CFRP composite materials are installed with piezoelectric sensors and the performance of the GWSHM system is quantified following the proposed hierarchical approach. The materials and layup are presented in Table 2. The panels made from the first two materials are quasi-isotropic whereas the panels made from the last material are anisotropic. The performance of the GWSHM system in a stiffened panel (500mm $\times$250mm) made from M21/TS800 in Table 2 is also quantified and presented.

Table 2: Material of flat plates specimens

Composition	Stacking sequence
H914-TS-5-134	$[0/90/ \pm 45]_{2s}$
PEEK/HTA-40	$[(0/90)/(\pm 45)/(0/90)/(\pm 45)/(0/90)]$
M21/TS800	$[\pm 45/0_2/90/0]_s$

3.1. Quasi-isotropic unidirectional CFRP panel

A flat panel (300 mm $\times$ 225 mm) is manufactured from unidirectional Hexply 914-TS-5-134 prepreg plies in the stacking sequence of $[0/90/ \pm 45]_{2s}$. Eight piezoelectric (DuraAct, PI ceramic) sensors are bonded to the surface of the panel using Hexcel Redux 312 epoxy based film adhesive, as shown in Figure 11(a). The coverage distribution resulting from this sensor network is presented in Figure 11(b).

Guided waves were excited with a five cycle Hanning-windowed tone burst at frequencies of 50, 100, 150, 200, 250, 300 and 350kHz. The highest amplitudes of the A0 wave mode and the S0 wave mode were observed in the sensor response to 50kHz and 300kHz excitation, respectively.

BVID was introduced by low velocity impact using an INSTRON CEAST 9350 drop tower. The panel was impacted at the same location three times with increasing energy of 4.8J, 6.41J and 7.84J. The formation of the BVID was confirmed using a handheld C-scan device (DolphiCam) as shown in Figure 11(c).
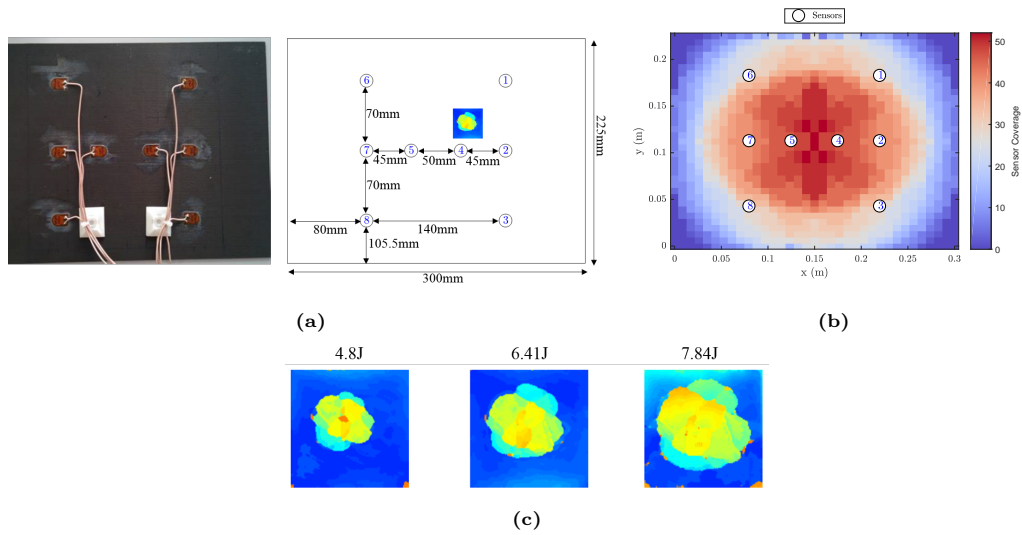
Figure 11: Quasi-isotropic unidirectional CFRP panel. (a) Sensor placement and (b) coverage. (c) C-scan image of BVID after each impact event. The image size is 35mm×35mm.
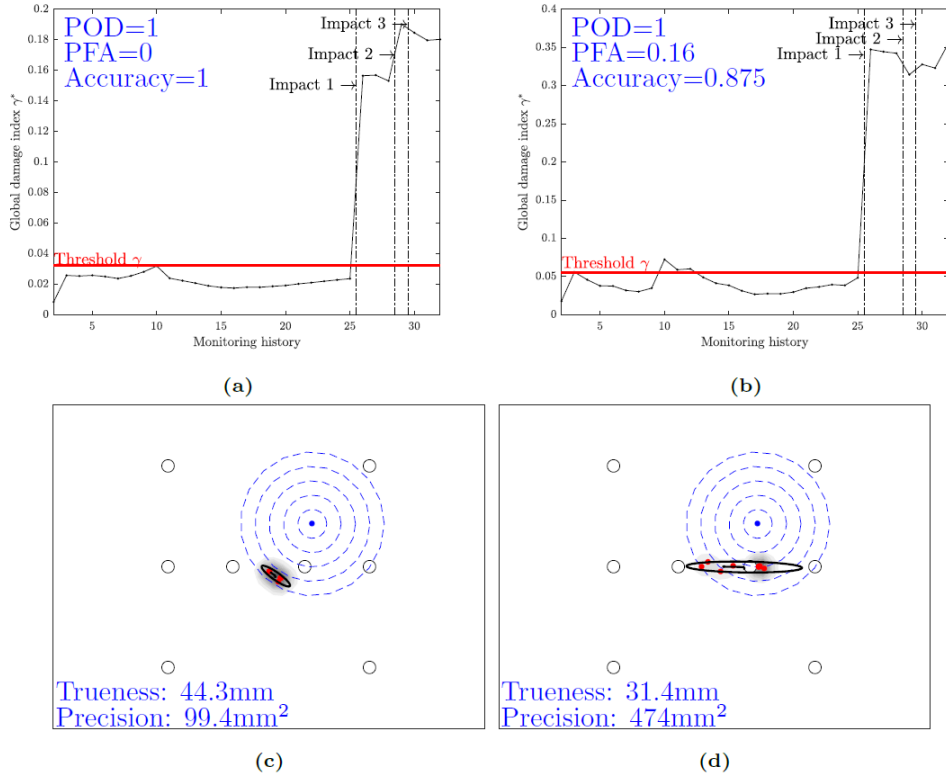
Figure 12: Damage identification results on the quasi-isotropic unidirectional CFRP panel. The monitoring history of the global damage index γ^* derived from guided wave response at (a) 50kHz and (b) 300kHz. Damage localisation results and performance quantification at (c) 50kHz and (d) 300kHz.

Before and after impact, guided wave measurements were collected 33 times from the sensor network on the panel in controlled laboratory conditions. The global damage index γ^* derived from each measurement is presented in Figures 12(a) and (b) The ambient temperature was monitored using four type K thermocouples and varied between $24°C$ and $26°C$. The first measurement before impact was used as the baseline signal. The first ten measurements recorded before impact were used for Level 1 noise quantification and threshold setting, and were excluded from the detection performance evaluation.

Damage detection performance is quantified using probability of detection (POD), probability of false alarm (PFA) and accuracy as defined in equations (2.3) and (2.3), and are presented on the top left corner of the Figures 12(a) and (b). Guided waves at both 50kHz and 300kHz are able to detect the occurrence of BVID with the predetermined threshold, POD = 1. However, at 300kHz, damage was incorrectly reported before damage was introduced, resulting in PFA = 0.16. Damage detection at 50kHz showed better accuracy (Accuracy = 1) compared to that at 300kHz (Accuracy = 0.875).

Damage localisation was performed for the positive detection cases shown in Figure 12(a)(b). Damage location was estimated using DAS at 50kHz and 300kHz and the localisation results are presented in Figure 12(c)(d). The impact location is marked by a blue dot surrounded by dash-line circles with radii from 10mm to 50mm for reference. The location estimates derived from each guided wave measurement are marked as red dots. The distribution area of the location estimates are represented using an ellipse centred at the mean coordinates of the estimates. The distance from impact location to the centre of the ellipse indicates the trueness of the estimations. The area of the ellipse represents the precision of the estimates. The value of trueness and precision are presented on the bottom left of each case. The trueness of estimates is around 33mm.

3.2. Quasi-isotropic woven CFRP panel

A quasi-isotropic laminate (300 mm × 225 mm) was made of woven fabric reinforced thermoplastic (PEEK/HTA40) plies in the stacking sequence $[(0/90)/(\pm45)/(0/90)/(\pm45)/(0/90)]$. Eight piezoelectric

(DuraAct, PI ceramic) sensors are bonded to the surface of the panel using thermoplastic film adhesive[34], as shown in Figure 13(a). The coverage distribution of the sensor network is presented in Figure 13(b).
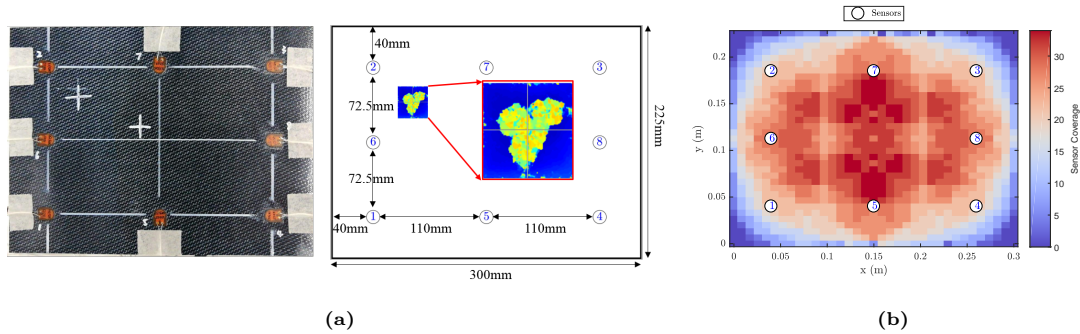

Figure 13: Quasi-isotropic woven CFRP panel: (a)Sensor placement and (b) sensor coverage.

In order to improve the data acquisition speed, instead of exciting guided waves using a Hanning window tone-burst signal centred at a single frequency, guided waves were excited using broad band linear chirp signals of frequency sweeping from 10 kHz to 600 kHz over a $200\mu s$ window. The recorded chirp signal responses were deconvoluted to Hanning window toneburst signals responses which are equivalent to the response of a guided wave to a toneburst excitation[35]. The highest amplitudes of the A0 wave mode and S0 wave mode were observed in the sensor response to 50kHz and 250kHz excitation.

BVID was introduced by low velocity impact using an INSTRON CEAST 9350 drop tower. The panel was impacted over a small region four times at 12J, introducing BVID over an area of 200mm×200mm. The formation of the BVID was confirmed using a handheld C-scan device (DolphiCam) as shown in Figure 13(a).

Before and after impact, guided wave measurements were collected 100 times from the sensor network on the panel in controlled laboratory conditions. The global damage index γ^*derived from each measurement is presented in Figures 14(a) and (b). The ambient temperature during the measurement was between 21°C and 23°C. The first signal recorded in pristine state was used as the baseline signal. The first twenty signals were used for Level 1 noise quantification and threshold setting and were excluded in damage detection assessment.

It can be seen that the global damage index at 250kHz fluctuated more than 50kHz, indicating that the S0 wave mode is more prone to variation in environmental conditions than the A0 wave mode. Impact damage was successfully detected at 50kHz with a detection accuracy of 1. Damage detection at 250kHz resulted a few cases of false negatives, which led to POD of 0.95 and detection accuracy of 0.975. BVID was located using DAS at 50kHz and 250kHz. The localisation results are presented in Figure 14(c)(d). DAS using guided wave responses at 50kHz provides the best trueness in the location estimates.
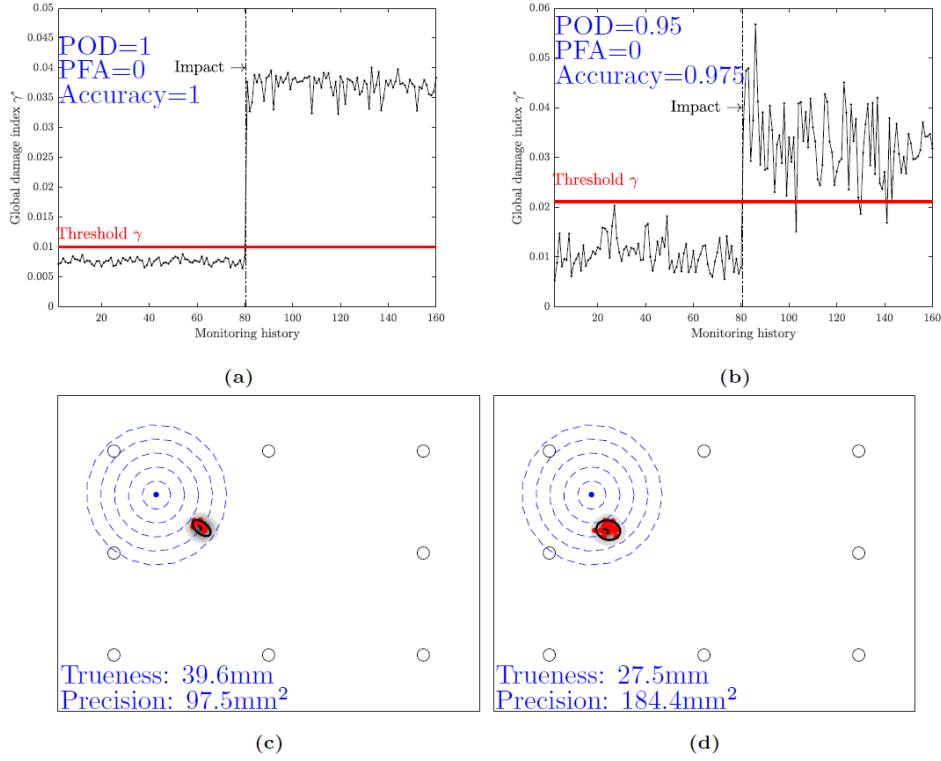
21

Figure 14: Damage identification results on the quasi-isotropic woven CFRP panel. Monitoring history of global damage index γ^* derived from guided wave response at (a) 50kHz and (b) 250kHz. Damage localisation results and performance quantification at (c) 50kHz and (d) 250kHz.

3.3. Anisotropic CFRP unidirectional laminate panels

Three 300 mm × 225 mm flat panels were manufactured from unidirectional M21/TS800 prepreg plies in the stacking sequence $[\pm 45/0_2/90/0]_s$. Eight piezoelectric (DuraAct, PI ceramic) sensors were attached to the surface of the panel using thermoplastic film adhesive[34], as shown in Figure 15(a). The coverage distribution resulting from the sensor network is presented in Figure 15(b). The highest amplitude of the A0 wave mode and the S0 wave mode were observed in the sensor response to 50kHz and 250kHz excitation.

BVID was introduced by a 20J low velocity impact using an INSTRON CEAST 9350 drop tower. The formation of the BVID was confirmed using a handheld C-scan device (DolphiCam). The location and energy of the impact events and C-scan of BVID on the three panels are shown in Figure 15(c). Before and after impact, guided wave signals were collected multiple times from the panel in controlled laboratory conditions. The global damage index γ^* derived from each measurement is presented in Figures 16. The ambient temperature varied between 21°C and 23°C. The first signal recorded before impact was used as the baseline signal. The first half of the signals recorded at pristine state were used for Level 1 noise quantification and threshold setting, and were excluded from the detection performance evaluation.
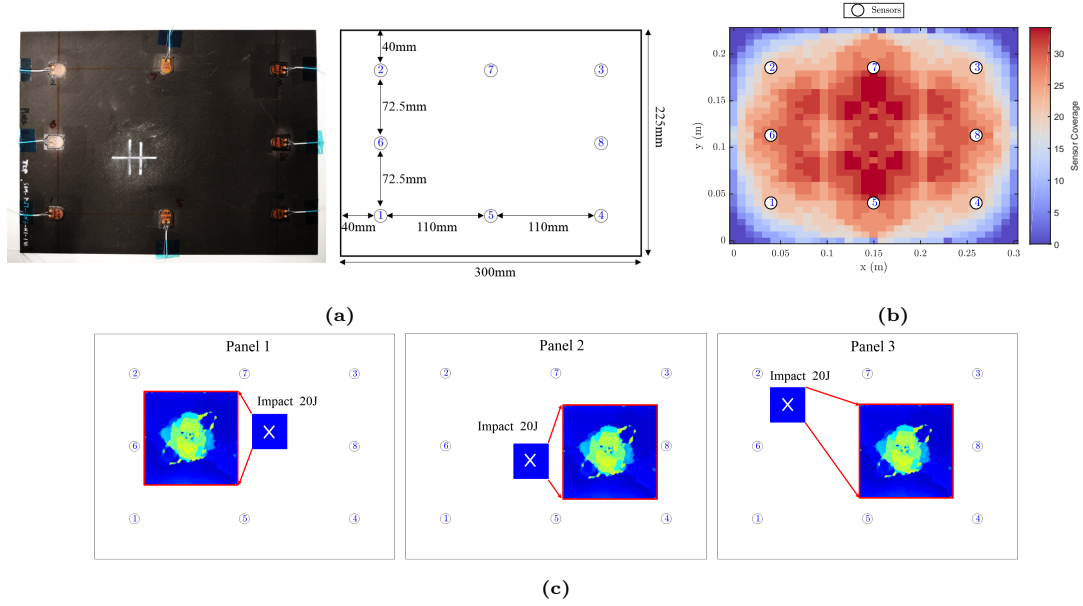
Figure 15: Anisotropic unidirectional CFRP panel. (a) sensor placement and (b) sensor coverage. (c) C-scan images of BVID after each impact event on three panels. The zoomed in area is 35mm×35mm.
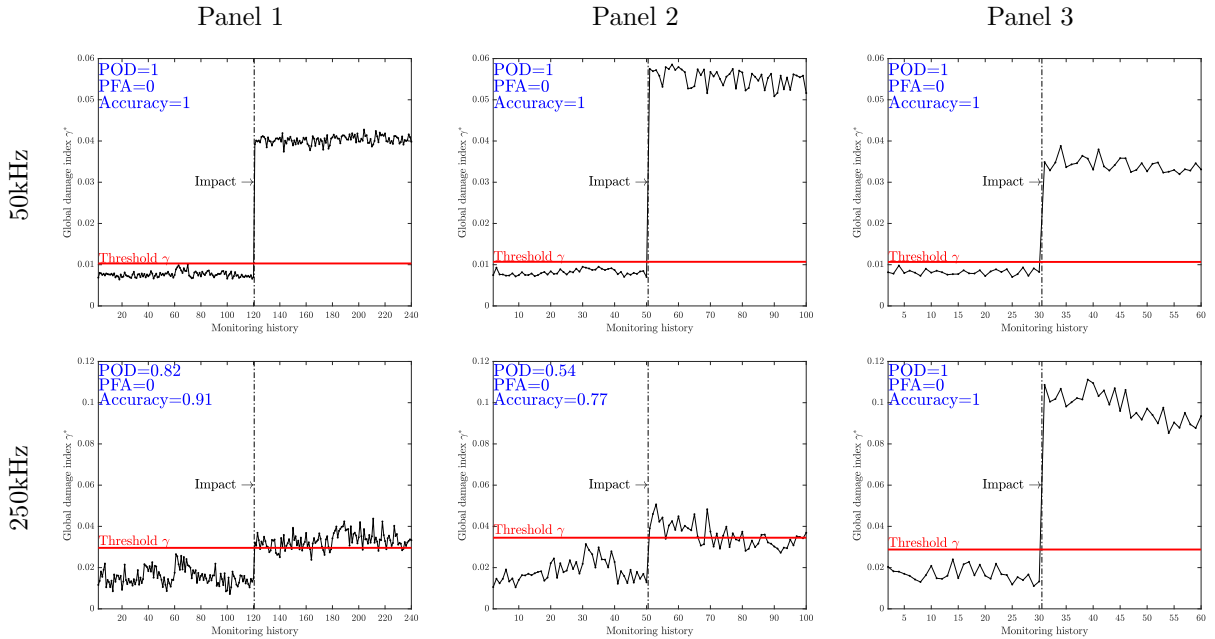

Figure 16: Monitoring history of global damage index γ^* on three anisotropic unidirectional CFRP panels at 50kHz and 250kHz.

The history of the global damage index γ^* at 50kHz and 250kHz is presented in Figure 16. The occurrence of the BVID in the three panels was correctly detected at 50kHz with detection accuracy of 1. The damage detection results at 250kHz on panels 1 and 2 showed many false negative cases, with POD of 0.82 and 0.54, respectively. This suggests that the guided wave response at 50kHz is more effective and reliable in detecting such BVID in this type of material.

The detected damage is localised using DAS at 50kHz and 250kHz. The damage localisation results in the three panels are presented in Figure 17. It can be seen that DAS using guided wave response at 50kHz provides the most accurate location estimates of BVID.
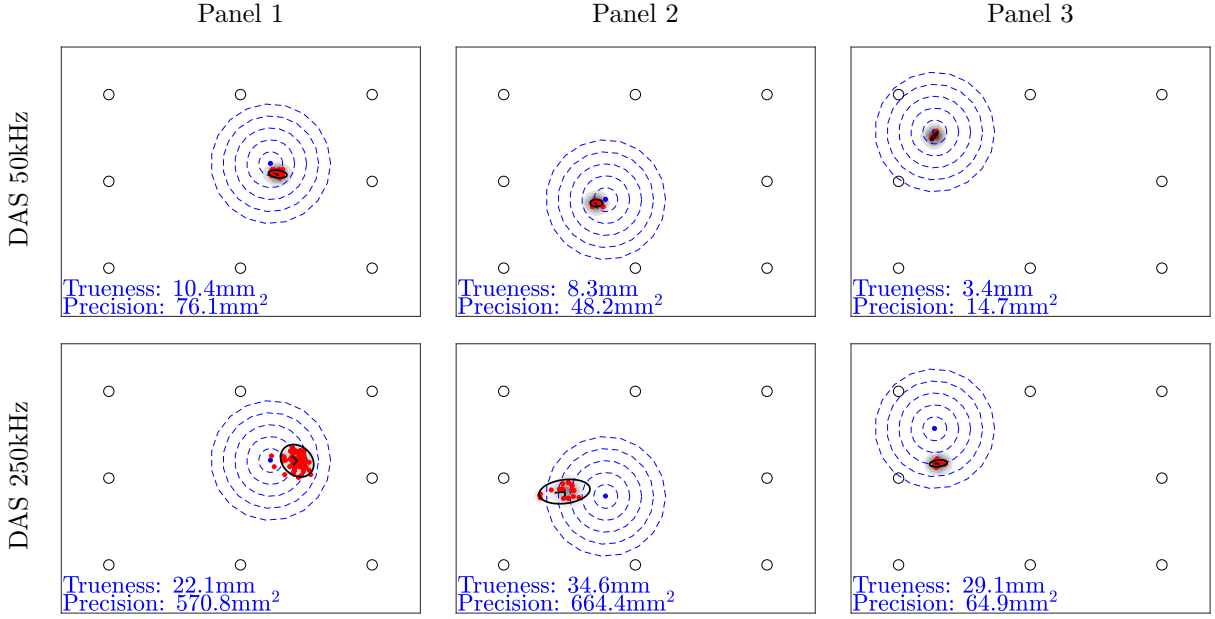
Figure 17: Damage localisation results and performance quantification on three anisotropic unidirectional CFRP panels at 50kHz and 250kHz.

A rectangular critical zone (140mm×65mm) is defined in the centre of the panel, as shown in 18.
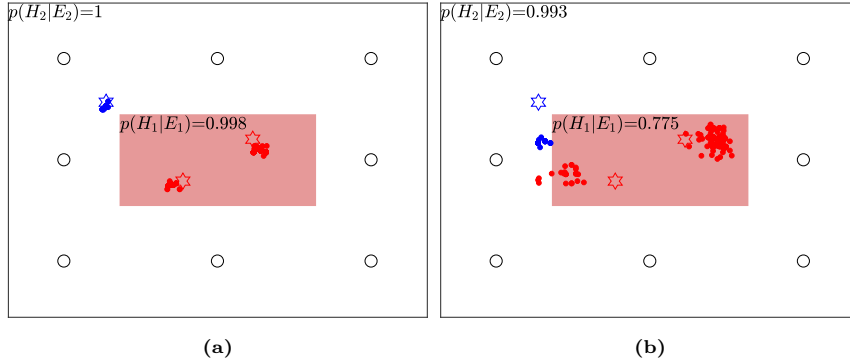

Figure 18: Probability of correctly indicating damage in a critical zone with guided waves at (a) 50kHz and (b) 250kHz.

Two out of three BVID locations are inside the critical zone. The location estimates of actual damage inside the rectangular critical zone are coloured in red. The location estimates of actual damage outside the rectangular critical zone are coloured by blue. The probability of correctly indicating damage within the critical zone is denoted as $p(H_1|E_1)$, where E_1 is the event of a damage location estimate inside the critical zone, H_1 is the hypothesis that the damage is located inside the critical zone. Likewise, the probability of correctly indicating damage outside the critical zone is denoted as $p(H_2|E_2)$, where E_2 is the event where a damage location estimate is located outside the critical zone, H_2 is the hypothesis that the damage is located outside the critical zone. The two probabilities, $p(H_1|E_1)$ and $p(H_2|E_2)$, are displayed in the corresponding zone in Figure 18. It can be seen that the DAS (50kHz) provides the highest probability of correctly locating damage that occurs in the critical zone.

3.4. Anisotropic unidirectional CFRP panel with an omega stiffener

A 500 mm × 250 mm flat panel with an omega-shaped stiffener was manufactured from unidirectional M21/TS800 prepreg plies in the stacking sequence of $[\pm45/0_2/90/0]_s$, as shown in Figure 19. The omega stiffener was made with same material as the flat panel and was co-bonded onto the flat panel

and consequently the thickness of the panel is doubled at the foot of the stiffener. Eight piezoelectric (DuraAct, PI ceramic) sensors were attached to the surface of the panel using thermoplastic film adhesive [34]. The coverage distribution resulting from the sensor network is presented in Figure 19.
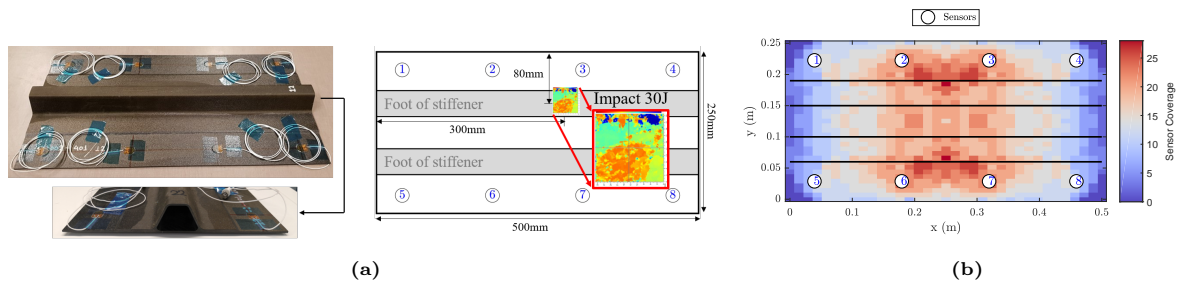

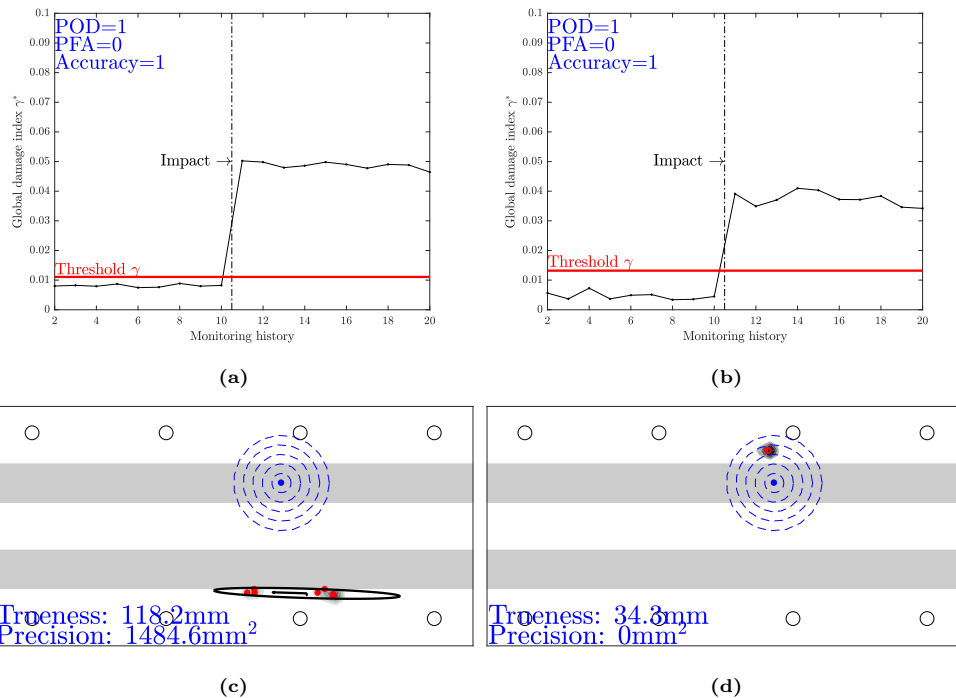**Figure 19:** Anisotropic unidirectional CFRP panel with an omega stiffener: (a) sensor placement and (b) sensor coverage.

Figure 20: Damage identification results on anisotropic unidirectional CFRP panel with omega stiffener. Monitoring history of global damage index γ^* at (a)50kHz and (b)250kHz. Damage localisation results and performance quantification at (c)50kHz and (d)250kHz.

BVID was introduced by a 30J impact at the foot of the stiffener, causing delamination of the skin and debonding between the foot of the stiffener and the skin, as shown in Figure 19(a). Before and after impact, guided wave signals were collected from the panel in controlled laboratory conditions. The global damage index γ^* derived from each measurement is presented in Figure 20. The ambient temperature varied between 21°C and 23°C. The first signal recorded before impact was used as the baseline signal. The first half of the signals recorded at pristine state were used for Level 1 noise quantification and threshold setting, and were excluded from the detection performance evaluation.

The occurrence of the BVID in the stiffened panel was correctly detected at both frequencies with a detection accuracy of 1. Unlike in simple panels, the damage localisation estimation at 250kHz is more accurate than that in 50kHz, which might be the result of the S0 guided wave (250kHz) being more sensitive to surface damage such as the debonding of the stiffener.

4. Quantification of GWSHM on CFRP components

This section presents the application and performance quantification of a GWSHM system on CFRP composite aircraft components in uncontrolled environmental conditions.

4.1. Experiment details

The components are flat anisotropic unidirectional CFRP panels installed with four CFRP omega stiffeners in the direction of the long side and three aluminium stringers in the direction of short side, as shown in Figure 21 (a). Three identical components were manufactured. The skin and the omega stiffeners are made from unidirectional M21/TS800 prepreg plies in the stacking sequence of $[\pm 45/0_2/90/0]_s$. The omega stiffeners were preformed and co-bonded onto the skin. The aluminium stringers were installed on to the panel using rivets.
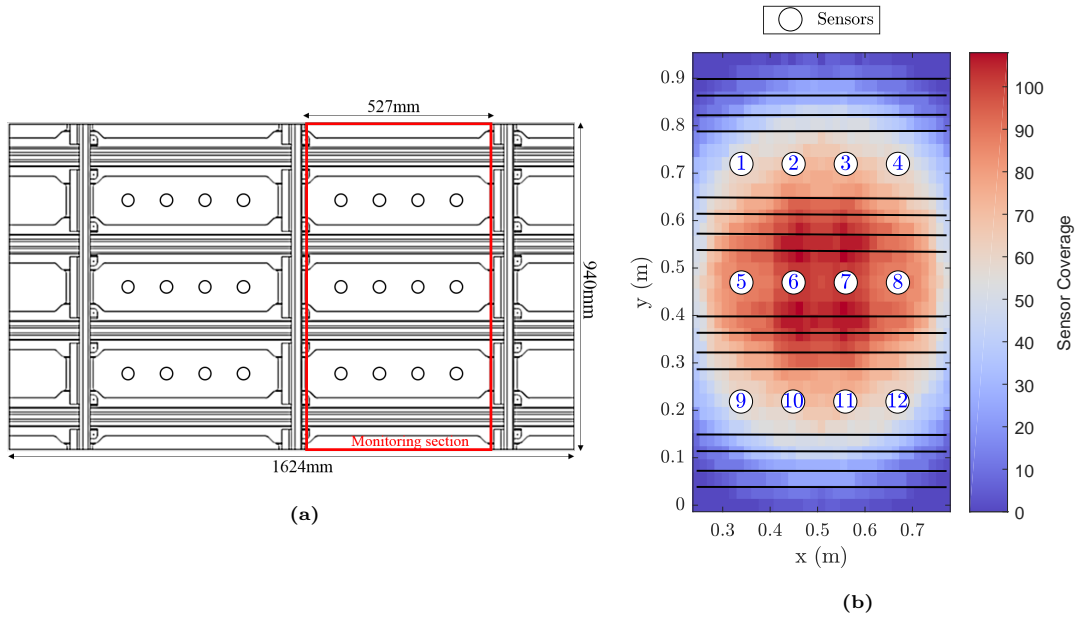
Figure 21: Flat stiffened panel with multiple stiffeners instrumented with DuraAct sensors: (a) sensor placement. (b) Sensor network coverage of the highlighted monitoring section.

A total number of 24 piezoelectric sensors (DuraAct, PI ceramic) sensors were bonded on the skin of the panel using thermoplastic film adhesive[34], as shown in Figure 21. Considering the channel limitation (12 channels) of the signal acquisition setup and the influence of the vertical aluminium stringer, the panel was divided into two 527mm×940mm monitoring sections separated by the middle vertical aluminium stringer with each area containing 12 sensors. The sensor network coverage on the monitoring section highlighted in Figure 21 (a) is shown in Figure 21 (b).

BVID was introduced by a low velocity weight drop impact with impactor mass of 5 kg. Two types of impact scenarios are considered: (a) impact on the outside of the panel during take off by flying runway debris, (b) impact on the inside of the panel during maintenance by dropped heavy tools. The set up to simulate the two impact scenarios is shown in Figure 22. The formation of the BVID was confirmed using a handheld C-scan device (DolphiCam).
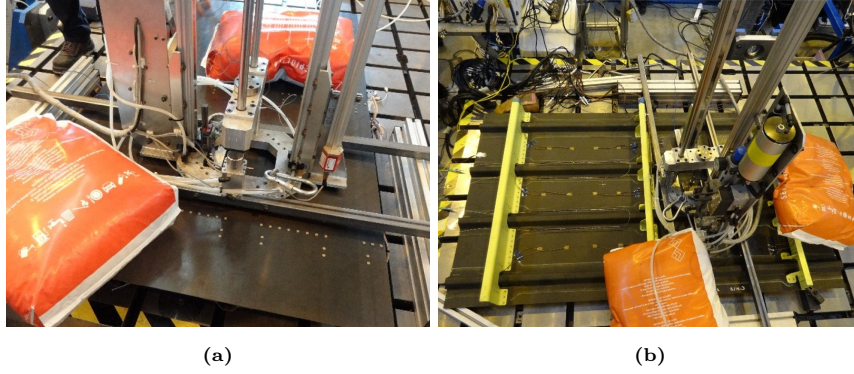
Figure 22: Impact setup. (a) Impact on the skin under the stiffener, simulating impact by runway debris. (b) Impact on the skin, simulating tool drop impact.

Panel 1 was impacted twice with 25J and 35J at the same position on the skin under the foot of omega stiffener, causing delamination of the skin and debonding of the stiffener, as shown in Figure 23(a). Panel 2 was impacted three times at different locations, as shown in Figure 23(b). The first impact (20J) was on the skin between under the stiffener, causing delamination of the skin. The second impact (35J) was on the skin between the feet of the stiffener, causing delamination of the skin and debonding of the stiffener. The third impact (20J) was on the skin, causing delamination of the skin.
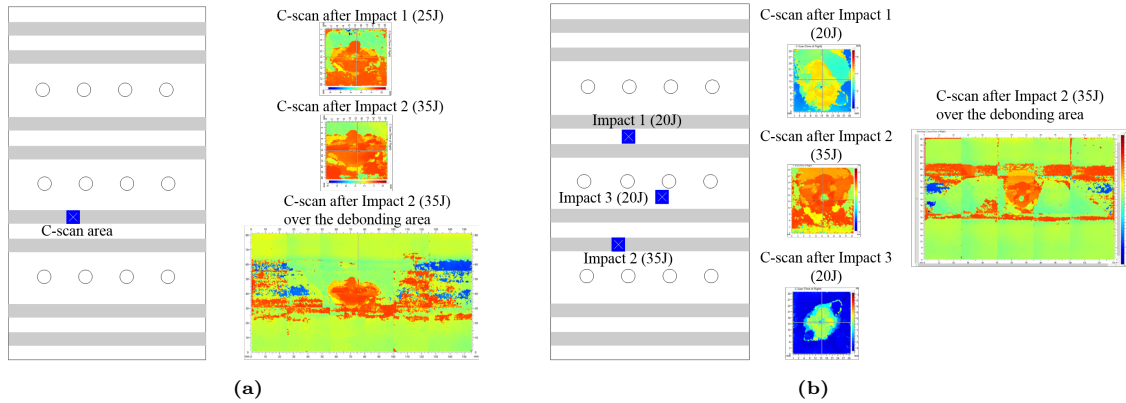

Figure 23: Impact location and C-scan after impact on (a) Panel 1 and (b) Panel 2.

4.2. Quantification of damage detection performance

Before and after impact, guided wave signals were collected a number of times from the panel in an open plan laboratory with no means of temperature control. The history of global damage index γ^* derived from each measurement is presented in Figures 24. The temperature of the panel was monitored using a type K thermocouple, and varied between 22°C and 27°C during the measurement. The first signal recorded before impact was used as the baseline signal. The first half of the signals recorded at pristine state were used for Level 1 noise quantification and threshold setting, and were excluded from detection performance evaluation. The damage detection threshold at 50kHz for the three panels is around 0.014. The damage detection threshold at 250kHz for the three panels is about 0.014.

The global damage index γ^* at 50kHz and 250kHz are presented in Figure 24. The occurrence of all BVID on the two panels was correctly detected without any false negatives at both frequencies. The resulting damage detection performance indices POD, PFA and accuracy are 1, 0 and 1, respectively. It can also be observed that, the global damage index showed significant change when new damage occurred. In particular, the global damage index obtained at 50kHz increased monotonically when new damage was introduced, which can be used to identify multiple damage sites and to select the baseline signal for locating multiple damage sites.
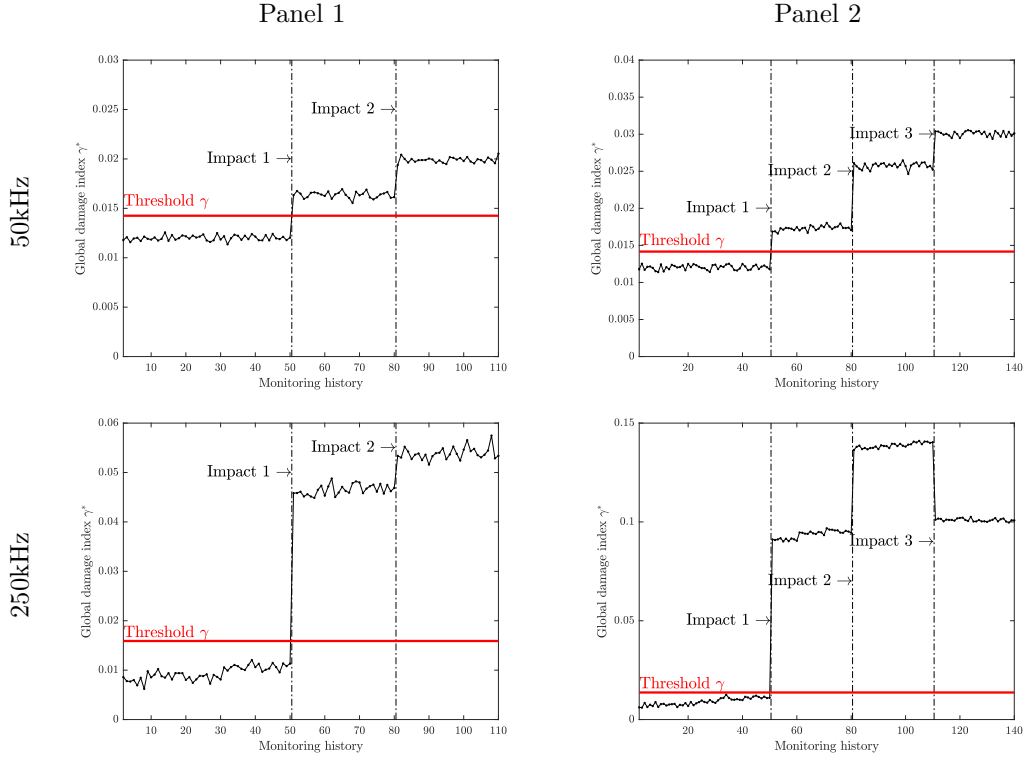
Figure 24: Monitoring history of global damage index γ^* on stiffened panels at 50kHz and 250kHz. For all cases, POD=1, PFA=0, Accuracy=1.

5. Conclusion

This paper proposes a multi-level hierarchical approach for establishing and assessing the performance of a GWSHM system for the detection and localisation of damage in CFRP composite structures. The hierarchical approach provides a systemic and practical way of establishing GWSHM systems for different structures in the presence of uncertainties and quantifies the system performance in four steps: (1) determining optimal sensor placement for the target structure, (2) threshold setting for a global damage index derived from the sensor network based on the noise level in the intended environmental and operations conditions, (3) detecting damage in critical locations and quantifying the probability of detection (POD), probability of false alarm (PFA) and detection accuracy and (4) locating the detected damage, quantifying the accuracy of location estimation and/or compute the probability of correctly indicating if damage is present in critical structural area.

The proposed approach was demonstrated for aircraft CFRP structures from coupon level (simple flat panels) to sub-component level (large flat panel with multiple CFRP stringers and aluminium frames). The detection and localisation of multiple barely visible impact damage was performed in three types of CFRP materials.

Acknowledgement

References

[1] V. Giurgiutiu, Structural health monitoring of aerospace composites, Academic Press, 2015.

[2] M. H. Aliabadi, Z. Sharif-Khodaei, Structural health monitoring for advanced composite structures, Vol. 8, World Scientific, 2017.

[3] Society of Automotive Engineers, Guidelines for implementation of structural health monitoring on fixed wing aircraft, SAE International, 2013.

[4] Z. Su, L. Ye, Identification of damage using Lamb waves: from fundamentals to applications, Vol. 48, Springer Science & Business Media, 2009.

[5] J. L. Rose, Waves in Plates, Cambridge University Press, 2014, p. 76–106. doi:10.1017/CBO9781107273610.008.

[6] N. Yue, M. H. Aliabadi, A scalable data-driven approach to temperature baseline reconstruction for guided wave structural health monitoring of anisotropic carbon-fibre-reinforced polymer structures, Structural Health Monitoring 0 (0) (0) 1475921719887109. doi:10.1177/1475921719887109.

[7] E. Monaco, V. Memmolo, F. Ricci, N. D. Boffa, L. Maio, Guided waves based SHM systems for composites structural elements: statistical analyses finalized at probability of detection definition and assessment, in: Health Monitoring of Structural and Biological Systems 2015, Vol. 9438, International Society for Optics and Photonics, 2015, p. 94380M.

[8] C. Annis, Mil-hdbk-1823a, Nondestructive Evaluation System Reliability Assessment. Department of Defense Handbook, Wright-Patterson AFB, USA (2009).

[9] T. Fawcett, An introduction to ROC analysis, Pattern recognition letters 27 (8) (2006) 861–874.

[10] C. M. Schubert Kabban, B. M. Greenwell, M. P. DeSimio, M. M. Derriso, The probability of detection for structural health monitoring systems: Repeated measures data, Structural Health Monitoring 14 (3) (2015) 252–264.

[11] V. Janapati, F. Kopsaftopoulos, F. Li, S. J. Lee, F.-K. Chang, Damage detection sensitivity characterization of acousto-ultrasound-based structural health monitoring techniques, Structural Health Monitoring 15 (2) (2016) 143–161.

[12] A. Gianneo, M. Carboni, M. Giglio, Feasibility study of a multi-parameter probability of detection formulation for a lamb waves–based structural health monitoring approach to light alloy aeronautical plates, Structural Health Monitoring 16 (2) (2017) 225–249.

[13] J. Moriot, N. Quaegebeur, A. Le Duff, P. Masson, A model-based approach for statistical assessment of detection and localization performance of guided wave–based imaging techniques, Structural Health Monitoring (2017) 1475921717744679.

[14] N. Yue, Z. Sharif-Khodaei, M. H. Aliabadi, Damage detectability model of pitch-catch configuration in composite plates, Key Engineering Materials 754 (2017) 387–390.

[15] J. Nichols, S. Trickey, M. Seaver, S. Motley, Using roc curves to assess the efficacy of several detectors of damage-induced nonlinearities in a bolted composite structure, Mechanical Systems and Signal Processing 22 (7) (2008) 1610–1622.

[16] Y. Lu, J. E. Michaels, Feature extraction and sensor fusion for ultrasonic structural health monitoring under changing environmental conditions, IEEE Sensors Journal 9 (11) (2009) 1462–1471.

[17] E. B. Flynn, M. D. Todd, A. J. Croxford, B. W. Drinkwater, P. D. Wilcox, Enhanced detection through low-order stochastic modeling for guided-wave structural health monitoring, Structural Health Monitoring 11 (2) (2012) 149–160.

[18] X. Zhao, H. Gao, G. Zhang, B. Ayhan, F. Yan, C. Kwan, J. L. Rose, Active health monitoring of an aircraft wing with embedded piezoelectric sensor/actuator network: I. defect detection, localization and growth monitoring, Smart Materials and Structures 16 (4) (2007) 1208–1217. `doi:10.1088/0964-1726/16/4/032`.

[19] J. E. Michaels, T. E. Michaels, Guided wave signal processing and image fusion for in situ damage localization in plates, Wave motion 44 (6) (2007) 482–492.

[20] J. E. Michaels, T. E. Michaels, Damage localization in inhomogeneous plates using a sparse array of ultrasonic transducers, in: AIP Conference Proceedings, Vol. 894, American Institute of Physics, 2007, pp. 846–853.

[21] E. B. Flynn, M. D. Todd, P. D. Wilcox, B. W. Drinkwater, A. J. Croxford, Maximum-likelihood estimation of damage location in guided-wave structural health monitoring, Proceedings of the Royal Society A: Mathematical, Physical and Engineering Sciences 467 (2133) (2011) 2575–2596. `doi:10.1098/rspa.2011.0095`.

[22] G. Yan, A bayesian approach for damage localization in plate-like structures using lamb waves, Smart Materials and Structures 22 (3) (2013) 035012.

[23] C. Fendzi, N. Mechbal, M. Rebillat, M. Guskov, G. Coffignal, A general bayesian framework for ellipse-based and hyperbola-based damage localization in anisotropic composite plates, Journal of Intelligent Material Systems and Structures 27 (3) (2016) 350–374.

[24] M. Thiene, Z. Sharif-Khodaei, M. H. Aliabadi, Optimal sensor placement for maximum area coverage (mac) for damage localization in composite structures, Smart materials and structures 25 (9) (2016) 095037.

[25] M. A. Pimentel, D. A. Clifton, L. Clifton, L. Tarassenko, A review of novelty detection, Signal Processing 99 (2014) 215–249.

[26] K. Worden, G. Manson, N. R. Fieller, Damage detection using outlier analysis, Journal of Sound and Vibration 229 (3) (2000) 647–667.

[27] K. Worden, S. G. Pierce, G. Manson, W. Philp, W. J. Staszewski, B. Culshaw, Detection of defects in composite plates using lamb waves and novelty detection, International Journal of Systems Science 31 (11) (2000) 1397–1409.

[28] Y.-J. Cha, Z. Wang, Unsupervised novelty detection–based structural damage localization using a density peaks-based fast clustering algorithm, Structural Health Monitoring 17 (2) (2018) 313–324.

[29] J. Moll, C.-P. Fritzen, Guided waves for autonomous online identification of structural defects under ambient temperature variations, Journal of Sound and Vibration 331 (20) (2012) 4587–4597.

[30] Z. Dworakowski, L. Ambrozinski, T. Stepinski, Multi-stage temperature compensation method for lamb wave measurements, Journal of Sound and Vibration 382 (2016) 328–339.

[31] J. E. Michaels, Detection, localization and characterization of damage in plates with an in situ array of spatially distributed ultrasonic sensors, Smart Materials and Structures 17 (3) (2008) 035035. `doi:10.1088/0964-1726/17/3/035035`.

[32] BS ISO 5725-1:1994 - Accuracy (trueness and precision) of measurement methods and results. General principles and definitions, 1995.

[33] BS ISO 5725-2:1994 - Accuracy (trueness and precision) of measurement methods and results. Basic methods for the determination of repeatability and reproducibility of a standard measurement method, 1995.

[34] N. Yue, Z. Sharif-Khodaei, M. H. Aliabadi, An innovative secondary bonding of sensors to composite structures for shm application, Key Engineering Materials 774 (2018) 516–522.

[35] J. E. Michaels, S. J. Lee, A. J. Croxford, P. D. Wilcox, Chirp excitation of ultrasonic guided waves, Ultrasonics 53 (1) (2013) 265–270.